MICROSTRUCTURE AND MAGNETIC PROPERTIES OF FePt/MgO MULTILAYERED THIN FILMS

By

Yang Fu

Thesis

Submitted to the Faculty of the

Graduate School of Vanderbilt University

in partial fulfillment of the requirements

for the degree of

MASTER OF SCIENCE

in

Interdisciplinary Materials Science

December, 2006

Nashville, Tennessee

Approved By

Dr. James E. Wittig

Dr. James Bentley

ACKNOWLEDGMENTS

I am grateful to all of those whom I have had pleasure to work with during this project and other related projects. Foremost, I would like to express my sincerest thanks to Professor James Wittig for his continuous guidance throughout my study at Vanderbilt University. As my advisor, Professor Wittig has taught and helped me more than I could ever give him credit for here. Without his help and financial support, the completion of this work would be impossible.

Secondly, I would like extend my endless thanks to Dr. James Bentley at Oak Ridge National Laboratory (ORNL). I appreciate all his tremendous help during my many visits to ORNL. I am grateful to his enormous contribution to this project as well as his invaluable comments and suggestions in academic research.

The financial support from Seagate Technology is greatly appreciated. Many thanks to Dr. Bin Lu for providing me the samples to complete this work and offering me a great internship opportunity at Seagate during 2005 summer. I am indebted to my supervisor, Dr. Yukiko Kubota, for teaching me how to prepare magnetic thin films. I appreciate all the assistance she provided during my ten week internship at Seagate.

The financial support from the ORNL SHaRE User Facility is also appreciated. I thank Carolyn Wells for setting me up as a SHaRE user and Dr. Neal Evans for technical support when needed at ORNL.

I also would like to thank Professor Weijie Lu and Dr. Senthil Sambandam for equipment support when sample preparation is needed at Fisk University.

Thanks to our staff, Sarah Satterwhite, Janell Lees and Lauren Fox who have always been there helping me with all the practical needs to complete this work. Thanks

to Carrie Gauchat for showing me the first steps in TEM sample preparation. Many thanks to Dr. Yingguo Peng and Dr. Jafar Al-Sharab for sharing their invaluable experiences in TEM sample preparation with me.

My special thanks are also dedicated to my friends, Xing Zhou, Siyu Wei, Ying Hu and Weiwei Zhang for all their continuous help and encouragement, and to the Vanderbilt University Chinese Student and Scholar Association for their assistance during my stay in Nashville.

Finally, I take this great opportunity to express my deep gratitude to my grandparents, parents, brothers and sisters for their endless support and encouragement. To reach this point in my life would not have been possible without their unconditional love.

TABLE OF CONTENTS

Page

ACKNOWLEDGMENTS ii

LIST OF TABLES vi

LIST OF FIGURES vii

Chapter

I. OBJECTIVE 1

II. INTRODUCTION 2

Background 2
Magnetic Materials for Data Storage 3
Hysteresis Loop and Magnetic Parameters 4
Magnetocrystalline Anisotropy 6
Longitudinal Magnetic Recording 7
Superparamagnetic Effect 9
Perpendicular Magnetic Recording 10
Perpendicular Magnetic Recording System 10
Perpendicular Magnetic Recording Media 12
Microstructure of Perpendicular Recording Media 12
Heat-Assisted Magnetic Recording 14
FePt Recording Media for Heat-Assisted Perpendicular Magnetic Recording 15
Thesis Overview 18

III. EXPERIMENTAL PROCEDURE 20

Preparation of FePt/MgO Multilayered Thin Films 20
Magnetic Property Measurements 21
Microstructure Characterization 22
TEM Sample Preparation 23
Conventional TEM 25
Energy-Filtered TEM 28
EDS Profiles 35

IV. RESULTS 37

Magnetic Properties 37
Microstructure Characterization 39
EDS Profiles 39

Electron Diffraction 40
Plan-View HRTEM images 46
Cross-Sectional BF and HRTEM images 48
Cross-Sectional EFTEM Images 52
Plan-View EFTEM Images 56

V. DISCUSSION 59

MgO Seedlayers 59
MgO/FePt Laminated Structure 59
Post-Deposition Annealing 61
Average Orientation of the Magnetic Easy Axis 62
Grain Size 63
Grain Separation 64
FePt Layer Continuity and Magnetic Properties 66

VI. CONCLUSIONS 67

VII. REFERENCES 68

LIST OF TABLES

Table Page

4.1 Magnetic properties of the annealed FePt/MgO multilayers 38

LIST OF FIGURES

Figure Page

2.1 Schematic drawing of a hysteresis loop. 5

2.2 Magnetization curves of a single HCP Co crystal measured in different directio.. 7

2.3 Longitudinal recording system. 8

2.4 Schematic drawing of the superparamagnetic effect 10

2.5 Structure of the cylindrical grains in perpendicular recording media 11

2.6 Perpendicular recording system 11

2.7 Principle of HAMR writing process 15

2.8 Schematic drawing shows annealing transforms FePt from disordered FCC phase to the ordered $L1_0$ phase 18

2.9 Schematic drawing shows the heteroepitaxial growth of [001] textured FePt films onto the [001] textured MgO seedlayers 18

3.1 Layer configuration of the FePt/MgO multilayered thin films. The FePt layer thickness X=2.5, 3.0, 3.5, and 4.0 nm 21

3.2 Perpendicular hysteresis loop of the annealed FePt/MgO multilayer with X=2.5 nm 22

3.3 Schematic diagram of the c-axis distribution angle 26

3.4 [001] zone axis (0^o tilt) SAD pattern of the annealed FePt/MgO multilayer with X=2.5 nm 27

3.5 SAD patterns for different specimen tilts of the annealed FePt/MgO multilayer with X=2.5 nm show the evolution of the diffraction patterns 27

3.6 Linear regression of $\sin(\omega_{hk0}/2)$ vs. $1/\sin\beta$ from the annealed FePt/MgO multilayer with X=2.5 nm reveals the c-axis distribution angle is 9^o 28

3.7 Schematic drawing of the Gatan imaging filter 30

3.8 Electron energy loss spectrum of Fe and O with three energy windows 31

3.9 Plan-view component EFTEM images for Fe in the annealed FePt/MgO multilayer with X=2.5 nm 32

3.10 Plan-view Fe map of the annealed FePt/MgO multilayer with X=2.5 nm 32

3.11 Plan-view component EFTEM images of O in the annealed FePt/MgO multilayer with X=2.5 nm 33

3.12 Plan-view O map of the annealed FePt/MgO multilayer with X=2.5 nm 33

3.13 Plan-view Fe jump-ratio image of the annealed FePt/MgO multilayer with X=2.5 nm 34

3.14 Plan-view O jump-ratio image of the annealed FePt/MgO multilayer with X=2.5 nm 35

3.15 EDS profiles of the as-deposited FePt/MgO multilayer with X=4.0 nm 36

4.1 Perpendicular hysteresis loops of the annealed FePt/MgO multilayers with X=2.5, 3.0, 3.5, 4.0 nm 37

4.2 EDS profiles of the as-deposited FePt/MgO multilayer with X=4.0 nm along the growth direction 39

4.3 SAD patterns of the as-deposited FePt/MgO multilayer with X=2.5 nm 40

4.4 SAD patterns of the as-deposited FePt/MgO multilayer with X=4.0 nm 41

4.5 SAD patterns of the annealed FePt/MgO multilayer with X=2.5 nm 42

4.6 The linear regression of $\sin(\omega_{hk0}/2)$ vs. $1/\sin\beta$ from the annealed FePt/MgO multilayer with X=2.5 nm 43

4.7 SAD patterns of the annealed FePt/MgO multilayer with X=4.0 nm 44

4.8 The linear regression of $\sin(\omega_{hk0}/2)$ vs. $1/\sin\beta$ from the annealed FePt/MgO multilayer with X=4.0 nm 45

4.9 Plan-view HRTEM images of the annealed FePt/MgO multilayer with X=2.5 nm 46

4.10 Plan-view HRTEM images of the annealed FePt/MgO multilayer with X=4.0 nm 47

4.11 Cross-sectional view BF images of the FePt/MgO multilayer with X=2.5 nm before (inset) and after annealing 48

4.12 Cross-sectional view HRTEM images of the FePt/MgO multilayer with X=2.5 nm 49

4.13 Cross-sectional view BF images of the FePt/MgO multilayer with X=4.0 nm before (inset) and after annealing 50

4.14 Cross-sectional view HRTEM images of the FePt/MgO multilayer with X=4.0 nm 51

4.15 Cross-sectional view EFTEM images of the as-deposited FePt/MgO multilayer with X=2.5 nm 52

4.16 Cross-sectional view EFTEM images of the annealed FePt/MgO multilayer with X=2.5 nm 52

4.17 Cross-sectional view EFTEM images of the as-deposited FePt/MgO multilayer with X=4.0 nm 54

4.18 Cross-sectional view EFTEM images of the annealed FePt/MgO multilayer with X=4.0 nm 55

4.19 Plan-view EFTEM images of the annealed FePt/MgO multilayer with X=2.5 nm 57

4.20 Plan-view EFTEM images of the annealed FePt/MgO multilayer with X=4.0 nm 58

5.1 Plan-view BF image of an annealed single layered FePt film 64

CHAPTER I

OBJECTIVE

FePt alloys with the CuAuI $L1_0$-ordered structure are important magnetic materials since their large uniaxial magnetocrystalline anisotropy ($K_u \sim 10^7 erg/cm^3$) can overcome the thermal stability problem of high-density magnetic recording media. However, to realize the application of FePt thin films as perpendicular recording media, the magnetic easy axis, which is the c-axis of the $L1_0$-ordered FePt, needs to be aligned normal to the film plane. It is known that [001] textured FePt thin films can be grown onto the [001] oriented MgO seedlayers and transformed from the disordered face centered cubic (FCC) phase to the $L1_0$-ordered phase upon annealing. However, high temperature annealing tends to degrade the [001] texture of single layered FePt films and causes the grains to coarsen forming large particles. Therefore, instead of growing a single layered FePt film, laminated FePt/MgO structures have been used to maintain the [001] texture and confine grain growth. In this research, transmission electron microscopy (TEM) and energy-filtered TEM (EFTEM) are employed to investigate the microstructure of a series of FePt/MgO multilayered thin films with different FePt layer thicknesses in order to better understand the influence of the microstructure on the corresponding magnetic properties.

CHAPTER II

INTRODUCTION

2.1 Background

The magnetic hard disk drive (HDD) is one of the most important components within the personal computer. Although new technology has made other data storage methods possible, magnetic recording still dominates data storage due to its fast speed and high recording density.

The first HDD in the world was built by IBM in 1956. It had fifty two-foot diameter disks assembled together featuring a total storage capacity of 5 Mbytes (1 byte = 1024 bits) at a recording density of 2 kbits/in^2. In the quest to lower the cost and improve the performance, the recording density has been increased more than 89 million-fold in the modern HDD. At present, the highest recording density in the commercial HDD is 179 Gbits/in^2, which enables two 2.5-inch platters assembled together to provide a total storage capacity of 200 Gbytes [1].

Today, the HDD industry's ability to increase recording density is more critical than ever as the requirements of HDD with large storage capacity continue to grow dramatically in the consumer electronics markets. However, continued growth in recording density not only challenges implementing new recording techniques to reduce the bit size on the disk surface, but also requires application of advanced materials for high-density recording media. Since the magnetic properties of the recording media are strongly influenced by the various features of their microstructure, optimization of the

magnetic properties through understanding structure-property correlations is of importance for developing high-density recording media.

2.2 Magnetic Materials for Data Storage

Magnetism in materials is caused by the spin of electrons and their orbital motion about their nuclei. Due to different electronic structures, materials can have different responses to an external magnetic field and thereby can be generally classified as diamagnetic, paramagnetic, ferromagnetic, antiferromagnetic and ferromagnetic materials. Among these, ferromagnetic materials are the most important for data storage due to their unique magnetic properties.

As compared with other magnetic materials, ferromagnetic materials have a large positive magnetic susceptibility. With such large susceptibilities, these materials can be easily magnetized as compared to other magnetic materials. This is because ferromagnetic materials exhibit a long-range ordering at the atomic level, which causes the unpaired electron spins to be lined up parallel with each other in a region called magnetic domain. Normally, these magnetic domains are randomly oriented with respect to one another at room temperature, resulting in no magnetism shown in the bulk materials. However, once exposed to a magnetic field, ferromagnetic materials can be easily magnetized by lining up the magnetic domains to the applied field. In addition, ferromagnetic materials tend to maintain their initial magnetization to some extent after the external field is removed. This extraordinary property of remembering the magnetic states has enabled a variety of applications of ferromagnetic materials in magnetic data storage.

Usually, Fe, Co, Ni and some of their alloys are ferromagnetic materials since the spins of the unpaired 3d electrons prefer to be aligned in the same direction by the magnetic exchange effect. At present, most present magnetic recording components, such as the writing heads and recording media, are composed of these materials.

2.3 Hysteresis Loop and Magnetic Parameters

For a ferromagnetic material, when it is magnetized in one direction, its magnetization will not relax back to zero even if the applied magnetic field is released. To remove the remanent magnetization, a field in the opposite direction is required. If the ferromagnetic material is exposed to an alternating magnetic field, its magnetization will trace out a hysteresis loop.

The hysteresis loop can be plot as the magnetization (M) or magnetic induction (B, where $B = H + 4\pi M$) versus the applied field (H). Figure 2.1 shows a typical magnetization curve (M vs. H). The important parameters which are usually used to quantify the magnetic properties of recording media are:

Saturation magnetization (M_s): M_s represents the condition where all the magnetic dipoles are aligned parallel to the magnetic field [2]. The magnitude of M_s is only dependent on the total number of the magnetic moments per unit volume. Therefore, M_s is an intrinsic material property and is usually sensitive to the chemical composition of the material.

Remanent magnetization (M_r): M_r is the value of magnetization when the external magnetic field is removed, i.e., $M_r = M|_{H=0}$. It reflects the strength of the ferromagnetic material to produce magnetic field.

Coercivity (H_c): H_c is defined as the value of the magnetic field where magnetization is zero ($H_c = H|_{M=0}$). It is a critical point on the magnetization curve where beyond this point the magnetization is switched to its opposite direction. H_c is an extrinsic property since it can be influenced by various microstructural features such as crystallographic texture and grain size.

Squareness ratio (S): S measures the squareness of the magnetization curve. It is defined as the ratio of M_r/M_s and has a maximum value of 1.

Hysteresis loop slope (α): α is defined as the slope of the magnetization curve evaluated at coercivity, $\alpha = 4\pi(dM/dH)|_{H=Hc}$ [3]. It measures the steepness of the magnetization curve during reversal process. Theoretical and experimental results have shown that α is related exchange coupling between magnetic grains. Usually, large value of α indicates a strong exchange coupling within the recording media [3].

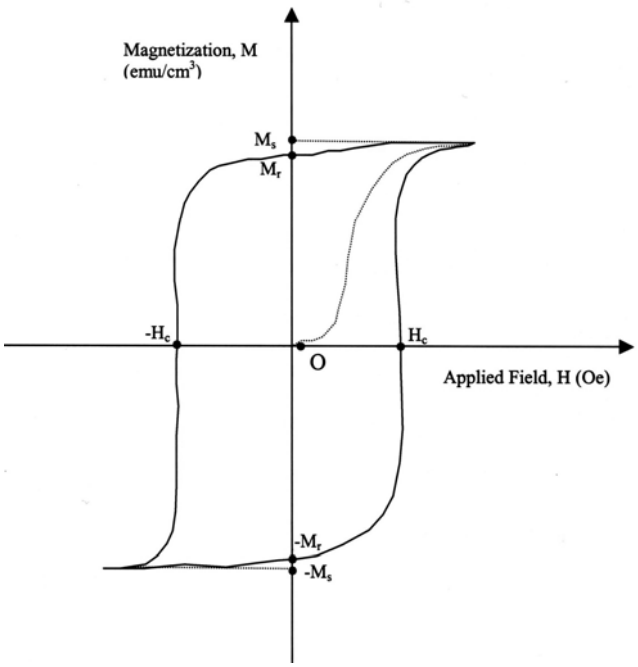

Figure 2.1 Schematic drawing of a hysteresis loop.

2.4 Magnetocrystalline Anisotropy

Ferromagnetic materials usually display different magnetic properties when an external field is applied in different directions. This dependence of magnetic property on direction is called magnetic anisotropy. There are several different types of anisotropy which are related to the crystal structure, the grain shape and the residual stress. Among these, only the crystal anisotropy, usually called magnetocrystalline anisotropy, is intrinsic to the material and is of practical importance to the design of magnetic recording media.

Magnetocrystalline anisotropy can be easily observed by measuring magnetization curves along different crystallographic directions. For example, for Co with a hexagonal closed packed (HCP) structure, which is commonly used in magnetic recording media, the magnetization curves in Figure 2.2 show that saturation can be easily achieved with a small field in the [0001] direction while a large field is required in the $[10\bar{1}0]$ direction. Therefore, the c-axis is the magnetic easy axis of HCP Co since less energy is required to line up the magnetic moments in this direction.

For a material with magnetocrystalline anisotropy, in the demagnetized state the magnetization vector tends to point along the direction of the easy axis. To deflect the magnetization from the easy axis, an applied field must do work against the anisotropy force. Therefore, there must be energy stored in the crystal when the magnetization points to a non-easy direction [2]. This energy is called magnetocrystalline anisotropy energy. For the ferromagnetic material which has only one magnetic easy axis, such as HCP Co and some of its alloys, the uniaxial magnetocrystalline anisotropy energy can be expressed as

$$E_{ua} = (K_0 + K_1 \sin^2\varphi + K_2 \sin^4\varphi + \ldots)V$$

where K_i is the magnetiocrystalline anisotropy constant, φ is the angle between the magnetic easy axis and the magnetization vector, and V is the magnetic grain volume [2]. Since K_0 is a constant and K_2 is usually very small, it is usually sufficient to express the uniaxial anisotropy energy as

$$E_{ua} = K_u V \sin^2\varphi$$

where K_u=K_1 and is called the uniaxial anisotropy constant [2].

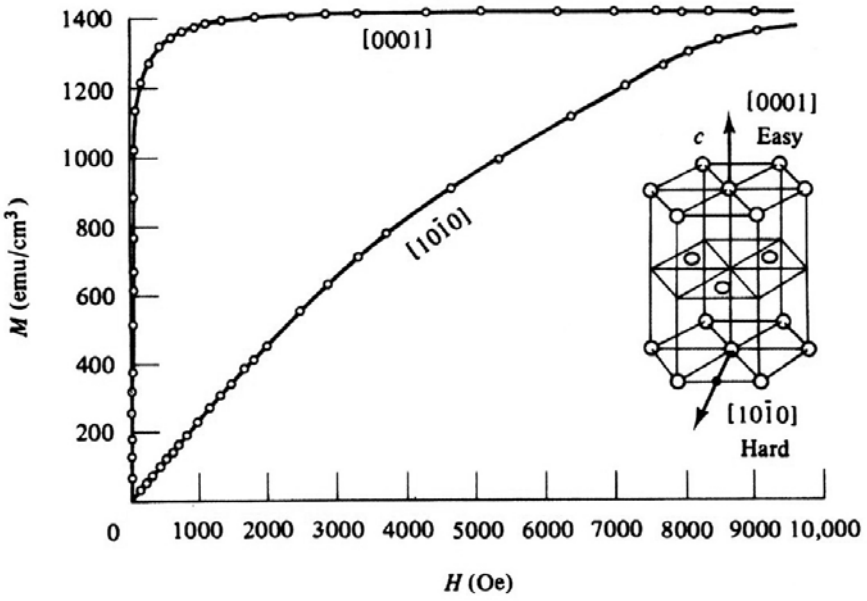

Figure 2.2 Magnetization curves of a single HCP Co crystal measured in different directions [2].

2.5 Longitudinal Magnetic Recording

In the present HDD markets, most products are based on longitudinal recording technologies where the magnetization of recorded bits lies in the plane of the disk. As shown in Figure 2.3, the longitudinal recording system contains a recording head

composed of a ring type writer and a reader flying in close proximity to a recording medium. The recording medium has a single magnetic storage layer and consists of weakly coupled magnetic grains. The common materials used in longitudinal recording media are CoCr alloys with additions of other elements such as Pt, Ta, and B. Since Cr tends to segregate at the grain boundaries in the CoCr based media, the magnetic grains are well separated from one another forming a granular microstructure which can effectively reduce the exchange coupling between the grains [4,5,6,7]. Therefore, by statistically averaging over several hundred weakly coupled magnetic grains per bit cell, high-density data storage and low noise are achieved in these longitudinal media.

However, continued growth in recording density requires scaling down the bit size, and thereby a reduction in the medium grain size is needed to maintain the read back signal-to-noise ratio (SNR). As the grain size is reduced, the magnetization of the grains may become unstable and can be reversed by thermal fluctuations resulting in data decay. This phenomenon is known as the superparamagnetic effect and has become increasingly important in recent years since new magnetic HDD products are designed for higher recording densities.

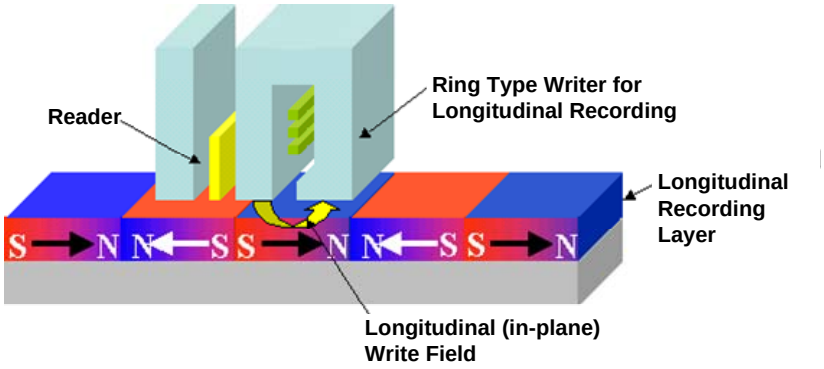

Figure 2.3 Longitudinal recording system [8].

2.6 Superparamagnetic Effect

The following simple model illustrates the superparamagnetic effect. For a single domain particle with uniaxial magnetocrystalline anisotropy, the energy barrier to reverse the magnetization is equal to the anisotropy energy E_{ua}, where $E_{ua} = K_uV$ ($\varphi = 0$ when magnetic moments are aligned along the magnetic easy axis). If the particle size becomes small enough, K_uV can be reduced to a value which is comparable to the ambient thermal energy (k_BT, where k_B is the Boltzman constant and T is the absolute temperature). As a result, thermal fluctuations can easily overcome the anisotropy forces and spontaneously reverse the magnetization from one easy direction to the other as shown in Figure 2.4. This magnetic reversal due to thermal fluctuation can occur even in the absence of a magnetic field, resulting in decay of the recorded signals. Therefore, in order to increase the thermal stability, high-density recording media must have a large anisotropy energy to minimize thermal fluctuation effects. Theoretical and experimental results have shown that to maintain sufficient signal stability over at least five years at drive operating temperatures T ~ 340K, the anisotropy energy K_uV must be larger than 55 k_BT [9,10]. This criterion sets an effective limit on the minimum grain volume of the current longitudinal recording media and predicts that recording densities can be limited by the thermal activation of the grains.

In the presence of the superparamanetic effect, there are a variety of material and system changes needed to lessen its impact. Currently, thermal stability can be improved by improving epitaxy [11], reduction of crystallographic defects [12], and most important of all by employing materials with higher magnetocrystalline anisotropy for the recording media [13]. However, most high K_u materials have very large coercivities that have

already exceeded the maximum writing capabilities of modern recording heads [13]. Therefore, new materials and architectures are needed for recording media, not only to maintain sufficient thermal stability but also to ease the write-field requirements at high recording densities.

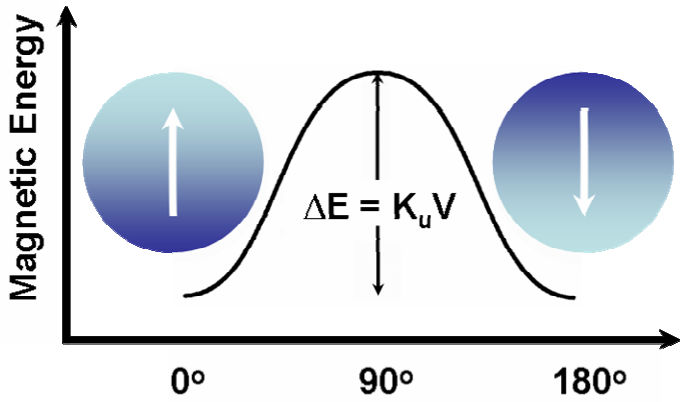

Figure 2.4 Schematic drawing of the superparamagnetic effect. When the anisotropy energy barrier of a single domain particle is comparable to the thermal energy, the magnetization can be reversed to its opposite direction without any external magnetic field.

2.7 Perpendicular Magnetic Recording

2.7.1 Perpendicular Magnetic Recording System

Unlike longitudinal media where the magnetic easy axes of the grains are oriented in the plane of the magnetic thin film, perpendicular media offer more advantages in terms of maximizing the number of thermally stable magnetic grains per unit area. This is because the magnetic grains in perpendicular media are oriented with their magnetic easy axes perpendicular to the film plane. The grains thereby can have small in-plane diameters while maintaining a large volume by forming cylindrical-like columns as shown in Figure 2.5. Therefore, this columnar structure in perpendicular recording media enables higher recording densities as compared to longitudinal media.

Figure 2.6 shows the configuration of a perpendicular recording system. Similar to the longitudinal recording system, the perpendicular recording system contains a recording head with a single pole writer and a reader flying above the recording media. However, since the magnetization of the recorded bits needs to be perpendicular to the disk surface, a magnetically soft under layer (SUL) is required to be grown under the recording media. This SUL is usually composed of materials with high permeability, high saturation magnetization and low coercivity, such as NiFe, CoNbB, FeAlSi and FeTaC, etc. Therefore, the SUL can be easily magnetized by the write pole and behaves like a mirror head to guide the magnetic flux from the write pole through the recording media.

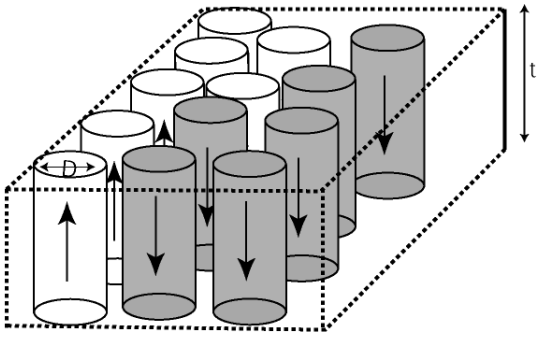

Figure 2.5 Structure of the cylindrical grains in perpendicular recording media, where D is the grain diameter and t is the grain height.

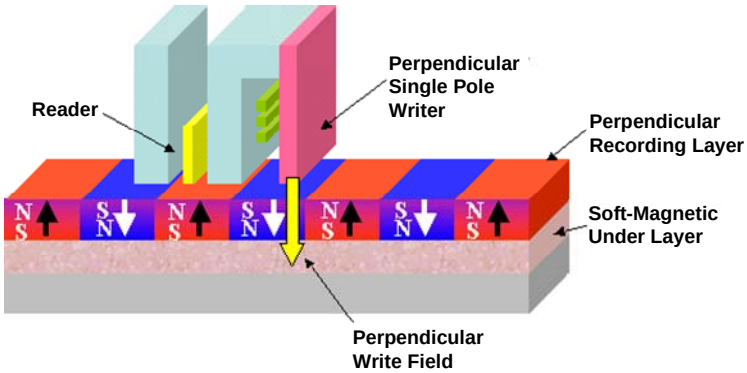

Figure 2.6 Perpendicular recording system [8].

2.7.2 Perpendicular Magnetic Recording Media

Since there is enormous experience in grain size control obtained for longitudinal media [14,15], CoCrPt alloys have been used in the first implementations of perpendicular recording media for the last few years. However, high concentrations of stacking faults present in the HCP Co grains may result in high thermal decay rates due to the reduction in magnetocrystalline anisotropy [6,16]. Recently, advances in deposition techniques have made it possible to grow well-defined superlattices, such as Co/Pd and Co/Pt multilayers [17,18], for perpendicular recording media. The advantage of employing multilayers as the recording media is that their magnetic properties can be tuned by adjusting the thickness of the individual layers as well as the total number of layers. However, as compared to granular recording media, these multilayered media have large transition noise due to the strong magnetic exchange coupling in the film plane. Therefore, a new type of perpendicular recording media with a combination of features of granular media and the multilayered media are of interest for high-density magnetic recording.

2.7.3 Microstructure of Perpendicular Recording Media

As magnetic recording changes from the longitudinal system to the perpendicular system, it is important to understand how the magnetic properties of the recording medium can be controlled by optimizing various features of the medium microstructure.

Crystallographic Texture

Perpendicular recording requires that the magnetic easy axis should be aligned normal to the thin film plane. This can be done by heteroepitaxially growing the recording layer

onto seedlayers that have specific textures. Since the orientation of the easy axis can have a strong influence on the magnetic properties of the recording layer, such as out-of-plane coercivity and remanent magnetization, it is important that the seedlayers possess very strong textures for initiating the growth of the recording layers with specific crystallographic orientations.

Grain Size and Distribution

Medium grain size and its distribution are important factors determining the read-back SNR. Since SNR is inversely proportional to the third power of grain size [19], scaling down the grain size as well as narrowing its distribution can effectively reduce the noise for high-density magnetic recording. However, the superparamagnetic effect has set limit on the minimum grain size for thermally stable media. Therefore, the media for high-density recording must consist of grains with modest sizes which can not only provide high SNR but also maintain sufficient thermal stability.

Grain Separation

The ideal microstructure for perpendicular recording media is that the magnetic grains are well isolated by nonmagnetic materials at the grain boundaries. This granular microstructure enables each grain to respond to the applied magnetic field independently, which in turn gives rise to high coercivity and low transition noise. In CoCr based recording media, grain separation is achieved by Cr segregation at the grain boundaries [4,5,6,7]. However, in the quest to increase the thermal stability, materials with higher magnetocrystalline anisotropy need to be employed in future perpendicular recording media. Therefore, it is necessary to discover new techniques to separate the magnetic grains in high-K_u recording media.

2.8 Heat-Assisted Magnetic Recording

Although perpendicular magnetic recording offers great advantages over longitudinal magnetic recording in terms of maximizing the number of thermally stable magnetic grains per unit area, it still cannot be extended to reach a recording density over 500 Gbits/in^2 due to the difficulty in maintaining sufficient SNR [20]. This is because the transition noise, usually referred to as jitter, is experimentally found to be the major factor limiting the SNR in perpendicular magnetic recording [19]. To reduce jitter, it is required to further scale down the medium grain size, which necessitates employing high-K_u materials to maintain thermal stability at higher recording densities. However, applying high-K_u materials, such as $SmCo_5$, FePt, and $Nd_2Fe_{14}B$, requires a write field which exceeds the maximum writing capabilities of present recoding heads [13,20,21]. In practice, even if the SUL can effectively double the write field during recording, the high-density perpendicular recording field is limited to 20 kOe [22]. Therefore, innovation of new recording technology is needed to sustain the continued growth in recording density.

In 1999, Katayama [23] and Saga [24] separately proposed a new magnetic recording system which is believed to be a promising alternative to increase the magnetic recording density beyond 500 Gbits/in^2 [20]. This new recording system combines the write field as used in conventional magnetic recording with the thermal writing as used in magneto-optical recording and thereby is named heat-assisted magnetic recording (HAMR).

In principle, HAMR takes advantage of the fact that magnetic properties such as saturation magnetization, magnetic anisotropy and covercivity decrease continuously to

zero when a ferromagnetic material is heated to its Curie temperature. By temporarily heating the recording media to an elevated temperature during the writing process, the coercivity of the recording medium can be reduced to a level where the magnetic grains can be easily magnetized by the write pole. Once the heated region is rapidly cooled back to ambient temperature while the write field is still applied, the data is stored in the recording media as shown in Figure 2.7. Therefore, HAMR allows the use of recording media with larger magnetocrystalline anisotropy as compared to that used in conventional perpendicular magnetic recording and accordingly provides enhanced thermal stability while scaling down the grain sizes.

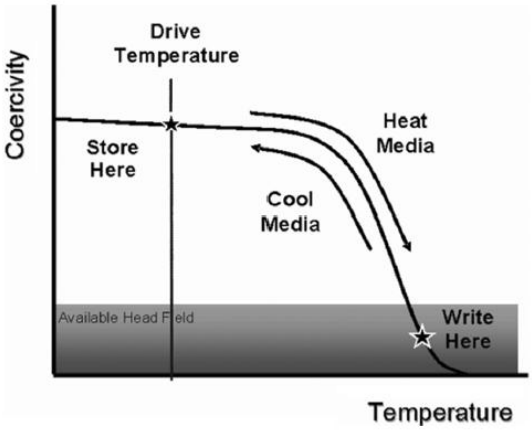

Figure 2.7 Principle of HAMR writing process [20].

2.9 FePt Recording Media for Heat-Assisted Perpendicular Magnetic Recording

In order to take full advantage of HAMR, the application of high K_u materials for data storage has been intensely pursued in recent years. Among these, FePt alloys with the CuAuI $L1_0$-ordered structure are promising candidate materials for heat-assisted perpendicular magnetic recording media since they have very large uniaxial

magnetocrystalline anisotropy (K_u ~ 10^7erg/cm^3). This magnetocrystalline anisotropy is 15 times larger than that of current HCP CoCr magnetic recording materials [25], and allows the recording media to have grains as small as ~ 3 nm without showing any superparamagnetic behavior.

However, as-deposited FePt thin films possess a disordered face-centered cubic (FCC) structure where the lattice points are randomly occupied by the Fe and Pt atoms. This disordered FCC FePt has no magnetocrystalline anisotropy and thereby cannot be used for magnetic recording. To transform FePt from the disordered FCC phase to the high-anisotropy $L1_0$ phase, high temperature annealing above 500^{o}C is usually required [26]. During annealing, the FCC cubic symmetry is broken by stacking of alternate planes of pure Fe and pure Pt along the c-axis while along the a-axis the planes still have a mixture of Fe and Pt atoms. As shown in Figure 2.8, this rearrangement of Fe and Pt atoms converts the crystal lattice from the disordered FCC structure to the ordered face-centered tetragonal (FCT) structure with a c/a ratio of ~ 0.96. Since the cubic symmetry is broken along the c-axis, large magnetocrystaline anisotropy is induced in this direction and thereby the c-axis becomes the magnetic easy axis.

To apply the $L1_0$-ordered FePt thin film to perpendicular magnetic recording, the magnetic easy axis must be aligned normal to the film plane. However, the FePt thin films deposited onto amorphous substrates tend to have a [111] texture since the (111) plane has the lowest surface energy. After this [111] textured FCC FePt thin film is annealed and transforms to the $L1_0$-ordered phase, the magnetic easy axis is tilted 35^o out of plane so that the expected large perpendicular anisotropy is greatly reduced [27]. Therefore, seedlayers such as Cr [28], Ag [29,30], B_2O_3 [31,32] and MgO [33,34] have

been applied to assist the FePt grains to be [001] oriented during deposition and maintain such texture during post annealing. Among these seedlayers, as-deposited MgO offers more advantages in seeding [001] oriented FePt thin films. This is because MgO has a cubic structure with a similar lattice spacing to the FCC FePt and can develop the [001] texture on amorphous substrates. As shown in Figure 2.9, the heteroepitaxial growth of [001] textured FePt thin film can be easily achieved by first depositing an MgO layer onto an amorphous substrate, followed by growing a FePt layer onto that MgO layer. Since the lattice misfit of the cubic MgO and the FCC FePt is 9.5%, the FePt lattice will tend to elongate in the film plane during annealing to reduce the misfit and residual stresses at the interface. Therefore, the FePt grains are mostly ordered along the [001] direction, which enables the film to possess large magnetic anisotropy perpendicular to the film plane.

In perpendicular magnetic recording, it is also required that the recording media must have a certain layer thickness to maintain a high enough magnetic flux for data storage. However, it is usually difficult to obtain a thick FePt film with a strong [001] texture since high temperature annealing tends to degrade the [001] texture of the single layered FePt films [34] and causes the grains to coalesce forming large particles [35]. Therefore, instead of growing a single thick FePt layer, an MgO/FePt laminated structure has been employed to prepare the highly [001] textred FePt thin films [34]. It is anticipated that after annealing, MgO will diffuse into the FePt layers and segregate at the grain boundaries forming granular media [34].

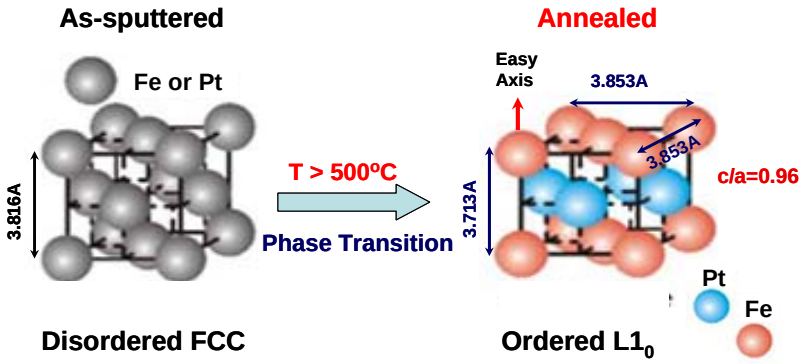

Figure 2.8 Schematic drawing shows annealing transforms FePt from disordered FCC phase to the ordered $L1_0$ phase.

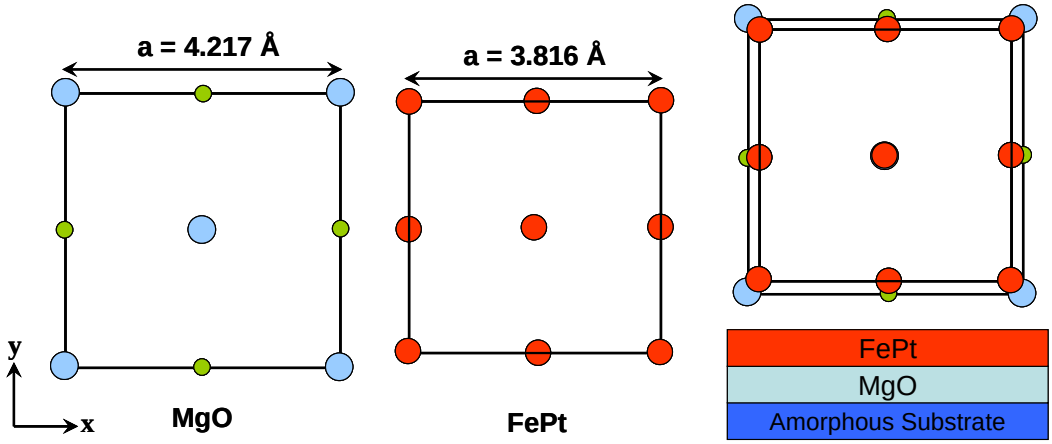

Figure 2.9 Schematic drawing shows the heteroepitaxial growth of [001] textured FePt films onto the [001] textured MgO seedlayers.

2.10 Thesis Overview

The main objective of this research is to study the microstructure and the magnetic properties of a series of FePt/MgO multilayered magnetic thin films. These multilayers are prepared under the same experimental conditions but with a variation in the FePt layer thickness. The microstructure of the FePt/MgO multilayers is characterized with transmission electron microscopy (TEM) and energy-filtered TEM (EFTEM). The

fundamental magnetic properties such as coercivity and squrareness ratio are measured and discussed through structure-property correlations.

CHAPTER III

EXPERIMENTAL PROCEDURE

3.1 Preparation of FePt/MgO Multilayered Thin Films

All the magnetic thin films involved in this research were prepared in collaboration with Seagate Technology (1251 Waterfront Place, Pittsburgh, PA 15222).

Four samples with different FePt layer thicknesses, 2.5, 3.0, 3.5 and 4.0 nm, were sputter deposited onto thermally oxidized single crystalline Si (001) substrates at ambient temperature with the a Unaxis M12 circulus sputtering system.

Figure 3.1 shows the configuration of the FePt/MgO multilayered thin films. All the MgO layers were produced by radio-frequency magnetron sputtering from MgO composite targets. The FePt magnetic layers were deposited by direct-current magnetron sputtering. The FePt layers were produced by first depositing a pure Fe layer onto the pre-deposited MgO layer, followed by depositing a pure Pt layer onto the Fe layer. The thicknesses of the Fe and Pt layers were carefully adjusted so that the composition of the FePt layers was kept at $Fe_{55}Pt_{45}$ for all the samples. To protect the magnetic thin films from oxidation, amorphous carbon layers with a thickness of 6 nm were coated onto the multilayers. After deposition, samples were annealed in a rapid thermal processing system with an Ar gas flow environment at 700 ^{o}C for 30 minutes.

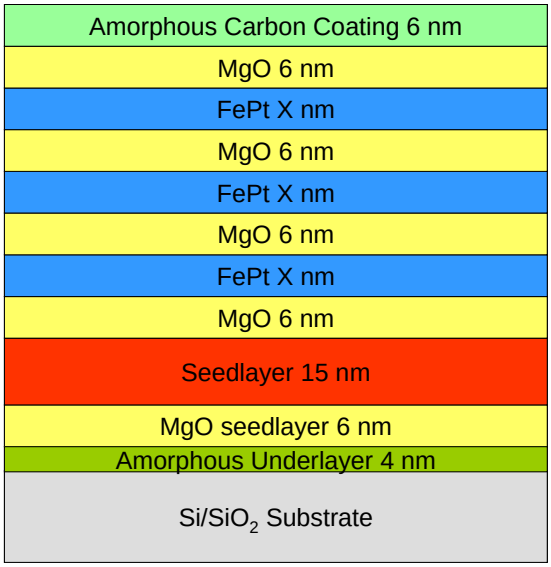

Figure 3.1 Layer configuration of the FePt/MgO multilayered thin films. The FePt layer thickness X=2.5, 3.0, 3.5, and 4.0 nm.

3.2 Magnetic Property Measurements

The magnetic properties of the annealed FePt/MgO multilayers were measured at room temperature using a Jasco polar Kerr magnetometer with a maximum field of 20 kOe. In a polar Kerr magnetometer, the specimen is placed between the poles of a strong electromagnet and magnetized perpendicularly to the thin film plane. During the magnetization process, a polarized laser beam is introduced perpendicularly to the film surface. Owing to the magneto-optical Kerr effect, the reflected laser beam has a polarization rotated slightly with respect to the incident beam. This slight rotation in polarization is called Kerr rotation and is proportional to the magnetic moments that have been lined up with the applied field in the specimen. In this research, in order to eliminate the influence from film thickness so that the magnetization of the specimens can be directly compared, normalized Kerr rotation angles are used to plot the hysteresis loops as shown in Figure 3.2, where the normalized Kerr rotation angle is defined as the Kerr

angle divided by the maximum Kerr angle. Since all the annealed FePt/MgO multilayers developed magnetic anisotropy perpendicular to the film plane, only the out-of-plane hysteresis loops were measured in this research.

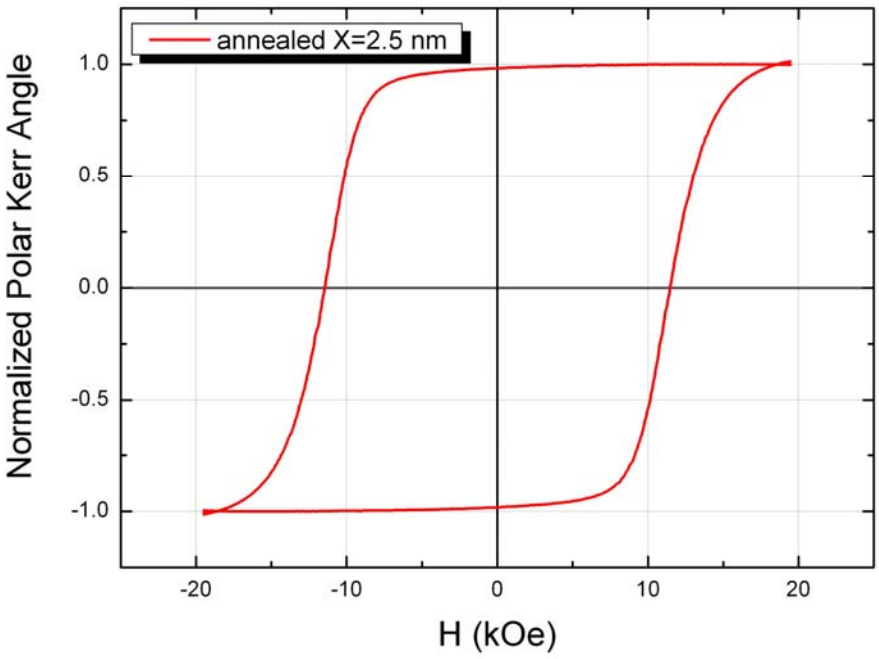

Figure 3.2 Perpendicular hysteresis loop of the annealed FePt/MgO multilayer with X=2.5 nm. H_c=15.6 kOe, S=0.99.

3.3 Microstructure Characterization

In this research, the microstructure of the FePt/MgO multilayers was characterized by transmission electron microscopy (TEM) with a combination of electron diffraction, bright-field (BF) imaging, high-resolution TEM (HRTEM) imaging, energy-filtered TEM (EFTEM) and energy-dispersive x-ray spectroscopy (EDS).

3.3.1 TEM Sample Preparation.

Sample Selection

Since the annealed FePt/MgO multilayers with X=2.5 and 4.0 nm exhibit the largest and smallest coercivities among all the multilayers, they were selected for microstructure characterization.

Plan-View Samples

Plan-view TEM samples were prepared using a conventional back-thinning method including mechanical grinding, dimpling and ion milling.

The sample was first mounted onto a metal holder using wax and ground from the back side with 240 grit SiC paper to a thickness of ~ 0.4 mm. Then a 3 mm diameter disk was cored out from the sample using a Fischione 330 ultrasonic disk cutter. The cored disk was thinned with 600 grit SiC paper to a thickness of ~ 100 μm. A Gatan 656 dimple-grinder was used to dimple the disk from the substrate side. By using a 15-mm-diameter brass polishing wheel with Buehler 6 μm diamond paste, Si was quickly removed with the table and arm rotating at speed setting 4. When a total dimple depth of ~ 70 μm was reached, a fine polishing was performed using a 15 mm felt polishing wheel and Buehler 1 μm diamond paste until the dimpled surface became very shinny (usually 3 ~ 4 minutes with the table and arm rotating at speed setting 4). The polished disk was cleaned with acetone and methanol before ion milling. A Fishione 1010 ion miller was used to back-thin the dimpled disk with the upper gun working at 4.0 kV and 5 mA. At the beginning of ion milling the incident beam angle was set at 15^{o}, then the incident angle was gradually reduced to 10^{o} before perforation. The average milling time until

perforation for a plan-view TEM sample was around 7 ~ 8 hours. During the milling process, the milling stage was cooled to –100^{o}C with liquid N_2 to reduce the ion-induced artifacts.

Cross-Sectional Samples

Cross-sectional samples were prepared by first gluing two pieces of identical bar shaped samples (~15 mm x 3.5 mm) together with Measurements Group M-610 bond. These two pieces of samples were cleaned with acetone and methanol before a very thin layer of M-610 bond was applied on both of the film surfaces. The glued sample was clamped and held on a hot plate to cure the M-610 bond at ~120^{o}C for 2 hours. Then the sample was thinned by diamond saw cutting and mechanical grinding until a cross section of 2.1 mm x 1.5 mm was obtained. The sample was cleaned again with acetone and methanol before it was inserted into a brass tube of 3 mm outer diameter and 2.5 mm inner diameter filled with EPO-TEK 301 epoxy bond. This epoxy bond is a mixture of two parts; the ratio of part A to part B is 8.5:1 drops. To cure the epoxy bond, the brass tube with the sample inside was placed on the hot plate at ~ 120^{o}C for about 2 ~ 3 minutes. A Buehler diamond saw was used to slice the brass tube into disks ~ 0.4 mm thick. One side of the disk was ground with 600 grit SiC paper and polished with 0.5 μm alumina slurry. Then the disk was thinned to ~ 100 μm from the unpolished side and dimpled until ~ 30 μm was left at the disk center using the same techniques as for preparation of plan-view samples. The final thinning of the cross-sectional samples was performed using the Fischione 1010 ion miller with both ion guns working at 4.0 kV and 5 mA. The milling angle was set at 12^{o} at the beginning and gradually reduced to 8^{o}

before perforation. Since the adhesive at the interface (M-610 bond) and the sample materials have different milling rates, the rotator of the specimen stage was rocked ± 45^{o} about the normal of the interface in order to produce an electron transparent area with uniform thickness. The average milling time until perforation for a cross-sectional sample was around 5 ~ 6 hours.

3.3.2 Conventional TEM

Conventional TEM imaging such as electron diffraction and BF imaging were performed with a Philips CM20 LaB_6 TEM working at 200 kV at Vanderbilt University. The HRTEM images were obtained using a Philips CM200-FEG TEM operating at 200 kV at Oak Ridge National Laboratory (ORNL).

Diffraction Tilting Technique for Film Texture Investigation

Since the magnetic properties of perpendicular magnetic recording media are strongly influenced by the orientation of the magnetic easy axis, it is important to know the quality of the c-axis orientation of the FePt/MgO multilayers. For perpendicular magnetic recording, the ideal case is that the c-axis is perfectly perpendicular to the film plane, i.e., all the grains are [001] oriented. However, in most cases, not all the grains are exactly [001] aligned during the non-equilibrium deposition process. Therefore, the average orientation of the c-axis is within a solid angle around the film normal as shown in Figure 3.3. This solid angle is defined as the c-axis distribution angle (θ) and can be used to study the quality of the film texture. Similar to the full width at half maximum

(FWHM) of an X-ray rocking curve, a larger distribution angle means a worse texture quality.

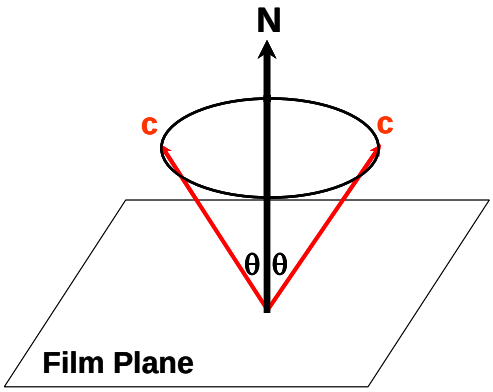

Figure 3.3 Schematic diagram of the c-axis distribution angle θ.

In this research, a diffraction tilting technique proposed by Tang etl. [36] was employed to study the c-axis distribution angle. The plan-view sample was first tilted to the [001] zone axis where the electron beam was perpendicular to the film surface (0^o tilt). Since most of the FePt and MgO grains were [001] oriented, the (hk0) reflections were present as rings with uniform intensity at 0^o tilt (Figure 3.4). Then SAD patterns were recorded at different sample tilt angles from 0^o to a large angle (usually $40^o \sim 60^o$). Figure 3.5 shows a typical evolution of the diffraction patterns from tilted samples. To calculate the c-axis distribution angle (θ), the angle subtended by (hk0) reflection arcs (ω_{hk0}) was measured with Adobe Photoshop software and plotted against the tilt angle (β) as shown in Figure 3.6. Since $\sin\theta = \sin(\omega_{hk0}/2)/\sin\beta$ [36], θ was determined from the slope of the linear regression of $\sin(\omega_{hk0}/2)$ vs. $1/\sin\beta$.

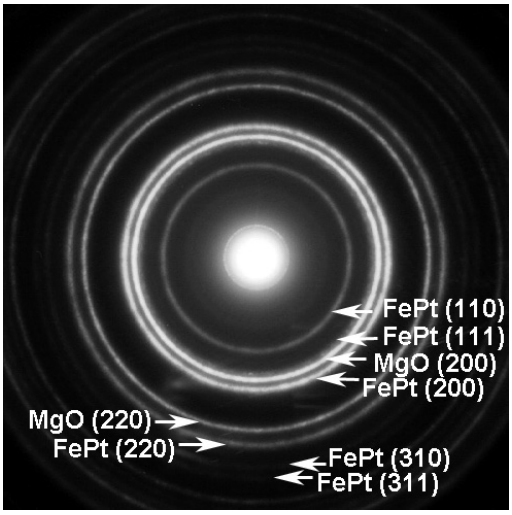

Figure 3.4 [001] zone axis (0^o tilt) SAD pattern of the annealed FePt/MgO multilayer with X=2.5 nm.

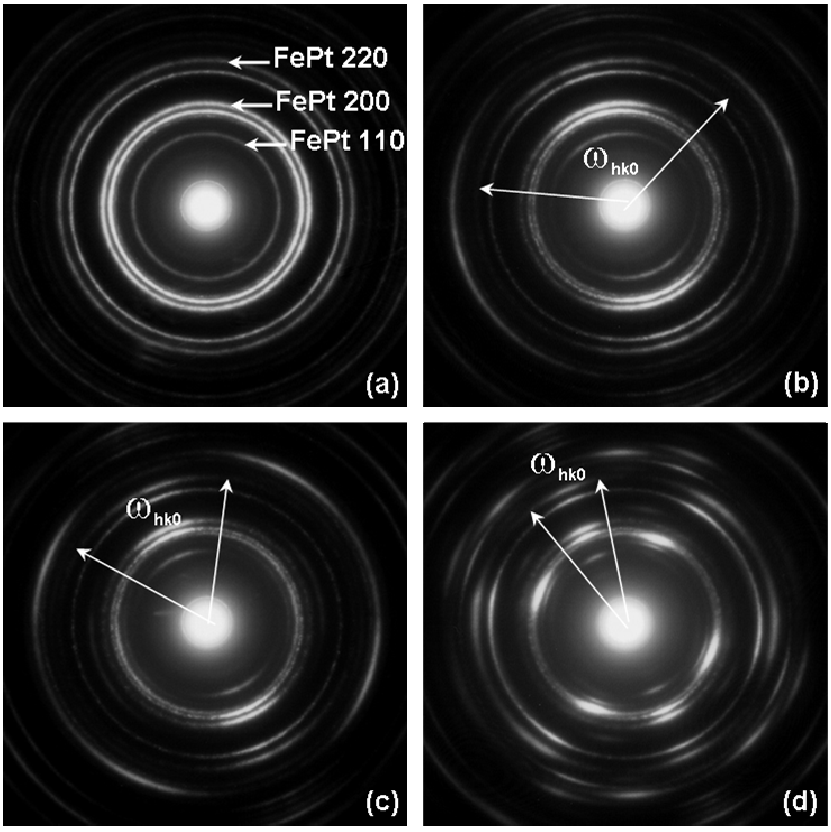

Figure 3.5 SAD patterns for different specimen tilts of the annealed FePt/MgO multilayer with X=2.5 nm show the evolution of the diffraction patterns. (a) 0^o, (b) 15^o, (c) 26^o, (d) 55^o tilt.

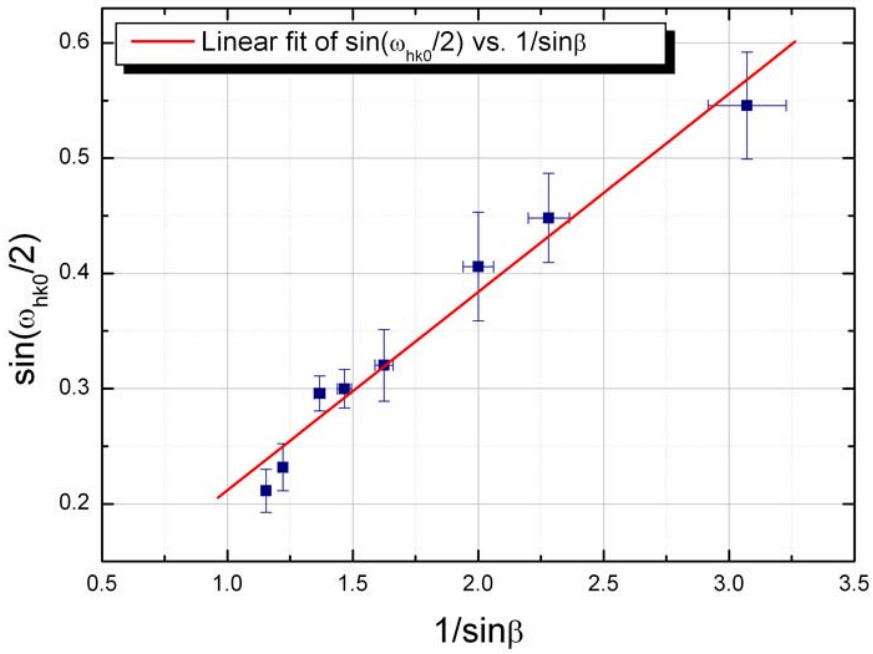

Figure 3.6 Linear regression of $\sin(\omega_{hk0}/2)$ vs. $1/\sin\beta$ from the annealed FePt/MgO multilayer with X=2.5 nm reveals the c-axis distribution angle is 9^{o}.

3.3.3 Energy-Filtered TEM

In addition to conventional TEM imaging techniques, energy-filtered TEM (EFETM) was used to assist understanding the microstructure of the FePt/MgO multilayers.

In principle, the EFTEM takes advantage of electron energy loss to form images. As the electron passes through the specimen, a certain amount of kinetic energy is lost due to electron-specimen interactions, including phonon and plasmon generation, inter- and intra-band transitions and inner-shell ionization [37]. When this transmitted electron beam is directed to a high resolution electron spectrometer, the electrons are separated by a magnetic prism according to their kinetic energy forming an electron energy loss

spectrum (EELS) where the intensity (number of electrons) is shown as a function of the electron energy loss. Therefore, with an imaging filter which is a specialized spectrometer, one can select electrons with certain amount of energy loss to produce images.

In this research, the EFTEM elemental-mapping was performed using a Philips CM30 TEM operating at 300kV equipped with a LaB_6 cathode and Gatan Imaging Filter (GIF) at ORNL. As shown in Figure 3.7, the GIF has a magnetic prism to disperse the electron energies and uses an adjustable slit which corresponds to an energy window to select electrons with a range of energies to form images. The energy window used for pre- and post-edge loss images was 30 eV while for zero-loss images it was 10 eV. All the EFTEM images are 512 x 512 pixels recorded with a 14-bit slow-scan charge coupled device (CCD) camera. With double binning and the ~ 20X magnification within the GIF, the 24 μm CCD pixel size is equivalent to ~ 0.6 nm at a TEM magnification of 4000X. Therefore each image has a recorded area of the specimen that is 307 nm x 307 nm.

For optimum elemental mapping, the Philips CM 30 TEM was set at the following working conditions:

incident beam divergence angle: $\alpha = 2.9$ mrad
collection semiangle: $\beta = 4.8$ mrad
electron probe current > 100 nA
TEM magnification: 4000X
exposure time: 10 ~ 15 sec

The spatial resolution of EFTEM elemental maps δ is determined by $\delta = C_c \frac{\Delta E}{E} \beta$, where

C_c: chromatic aberration coefficient of the objective lens
ΔE: slit width
E: beam energy
β: collection semiangle

In this research, the spatial resolution is determined to be 0.96 nm with C_c = ~ 2 mm, ΔE= 30 eV, E = 300 eV and β = 4.8 mrad.

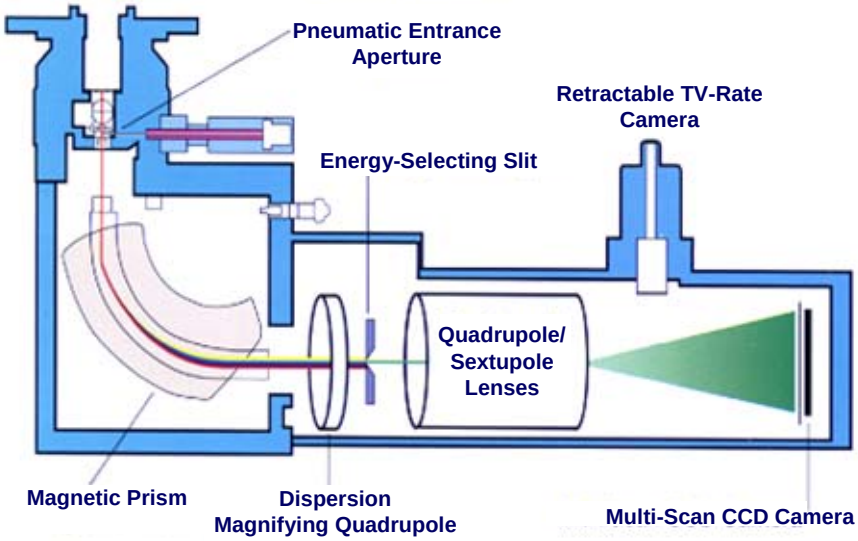

Figure 3.7 Schematic drawing of the Gatan imaging filter.

EFTEM Image Processing

The EFTEM images acquired in this research include pre- and post-edge Fe L_{23} core loss and O K core loss. With DigitalMicrograph software, these component images were first aligned using a cross-correlation procedure for drift correction and further processed to produce elemental maps and jump-ratio images.

Elemental Maps

The elemental map is the spatial variation of the core-loss intensity of an element in the specimen. In this research, a conventional three-window method was employed to produce elemental maps.

Figure 3.8 shows an enlarged portion of an electron energy loss spectrum with two sets of three energy windows around the Fe L_{23} edge and the O K edge. Each window is 30 eV in width.

Figure 3.9 shows an example of pre-edge 1, pre-edge 2 and post-edge images of the Fe L_{23} core loss. The two pre-edge images are used to calculate the background by using the power law fitting at each pixel:

$$I_{background} = AE^{-r}$$

where A and r are the fitting parameters, and E is the energy loss of the electrons. This modeled background is then subtracted pixel by pixel from the post-edge image to produce the Fe map as shown in Figure 3.10.

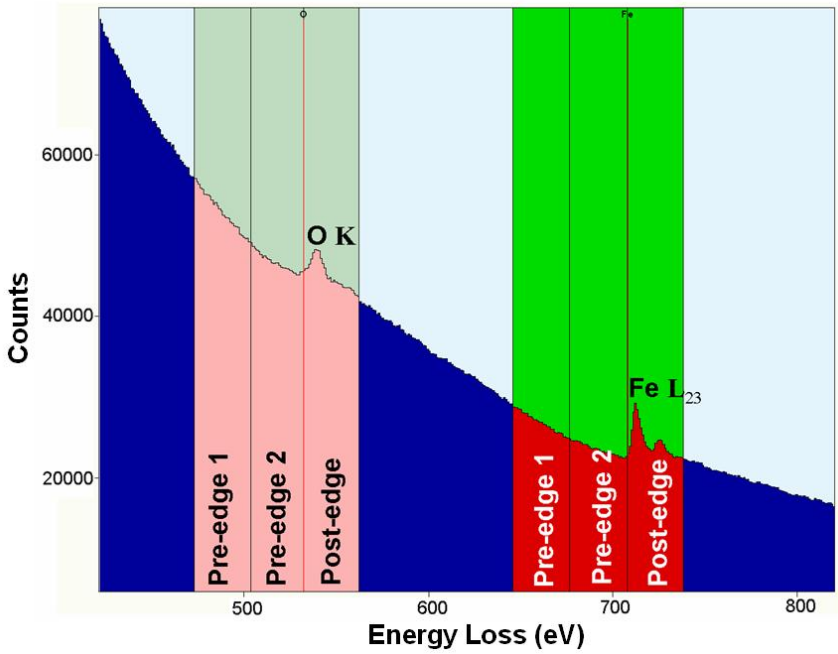

Figure 3.8 Electron energy loss spectrum of Fe and O with three energy windows.

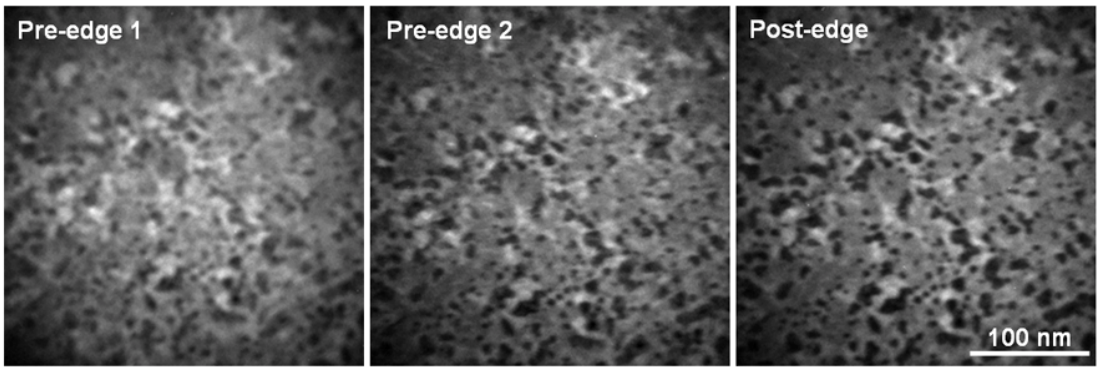

Figure 3.9 Plan-view component EFTEM images for Fe in the annealed FePt/MgO multilayer with X=2.5 nm.

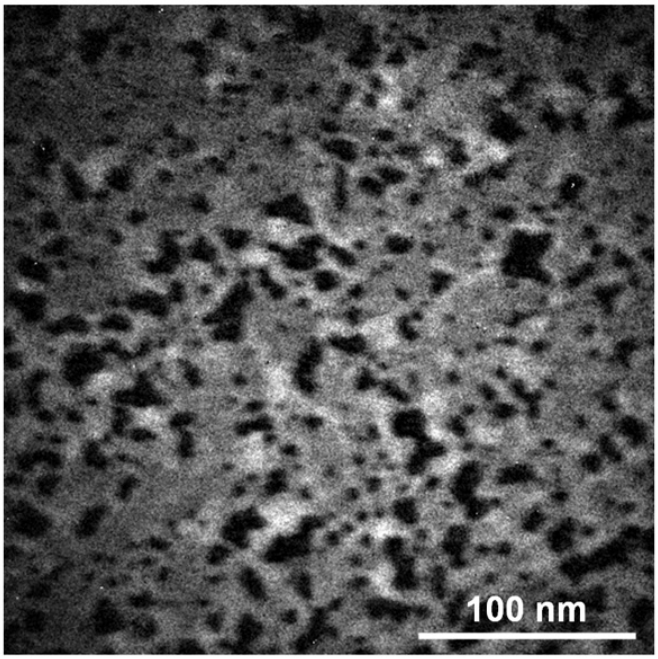

Figure 3.10 Plan-view Fe map of the annealed FePt/MgO multilayer with X=2.5 nm.

Figure 3.11 shows an example of pre-edge 1, pre-edge 2 and post-edge images for the O K core loss. The O map (Figure 3.12) is produced in the same way as the Fe map.

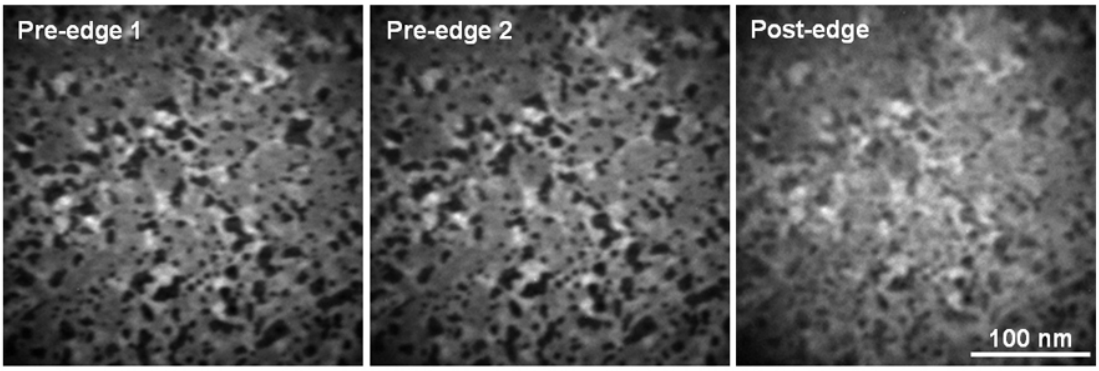

Figure 3.11 Plan-view component EFTEM images of O in the annealed FePt/MgO multilayer with X=2.5 nm.

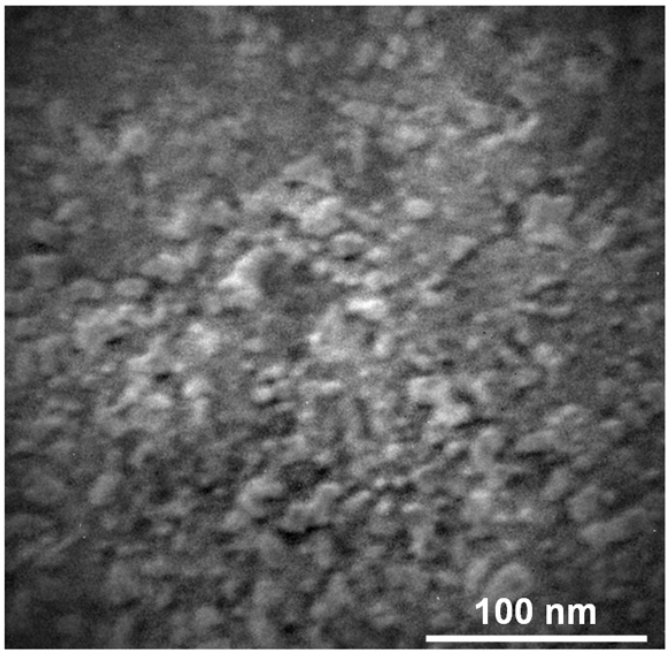

Figure 3.12 Plan-view O map of the annealed FePt/MgO multilayer with X=2.5 nm.

Jump-Ratio Images

In addition to elemental maps, jump-ratio images also provide qualitative information about the sample composition. To obtain jump-ratio images, the pixel intensity in the post-edge image is divided by the corresponding pixel intensity in the pre-edge 2 image. This pixel-by-pixel division effectively reduces the influences of diffraction contrast and variation in sample thickness. Figure 3.13 and Figure 3.14 respectively show jump-ratio images of Fe and O in the annealed FePt/MgO multilayer with X=2.5 nm.

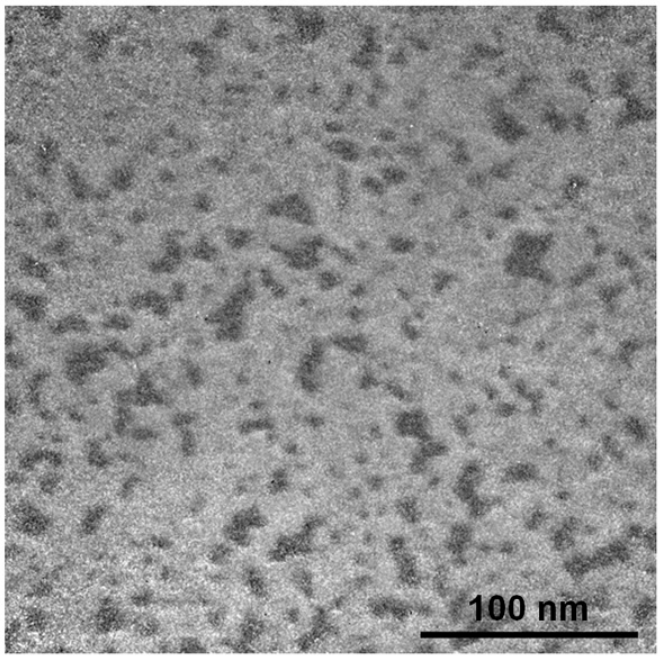

Figure 3.13 Plan-view Fe jump-ratio image of the annealed FePt/MgO multilayer with X=2.5 nm.

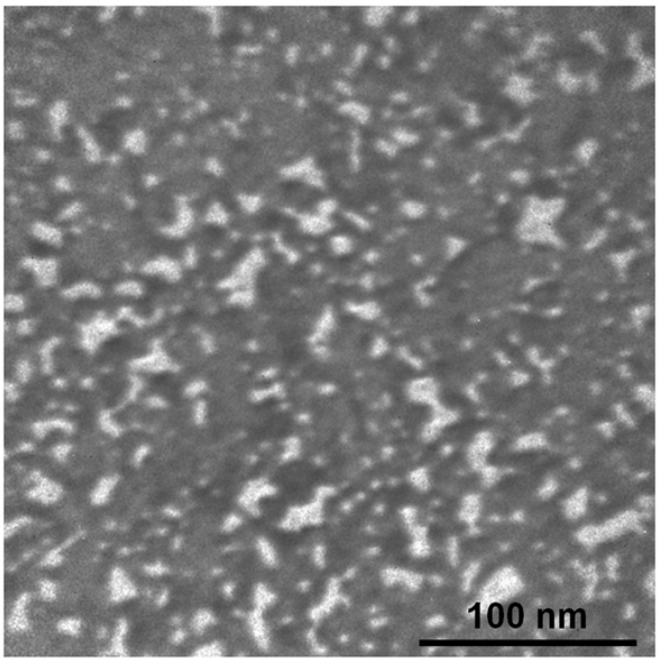

Figure 3.14 Plan-view O jump-ratio image of the annealed FePt/MgO multilayer with X=2.5 nm.

3.3.4 EDS Profiles

The EDS profiles were obtained with a Philips CM200-FEG TEM operating at 200 kV in the STEM mode at ORNL. The scanning electron probe was ~ 1.6 nm in diameter and the probe current was ~ 1 nA. To precisely control the positioning of the electron probe and correct for probe and specimen drift during acquisition, Emispec Vision software was used. In this research, EDS profiles of Mg K_α, Fe K_α and Pt L_α lines were measured from only the cross-sectional samples. Figure 3.15 shows the EDS profiles along the growth direction of the as-deposited FePt/MgO multilayer with X=4.0 nm. The total profile length is 40 nm in 1 nm steps, and the acquisition time for each probe position was 5 seconds.

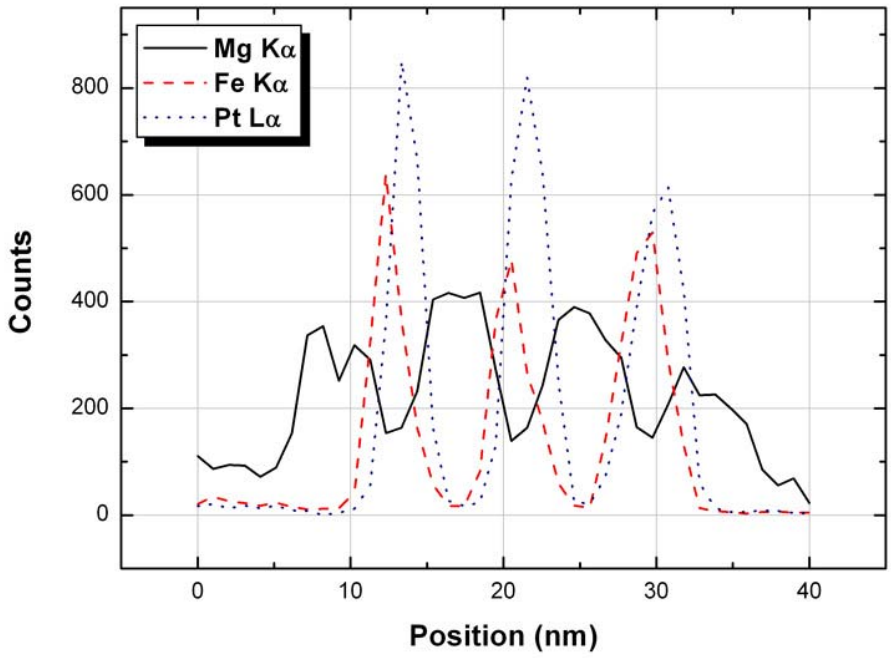

Figure 3.15 EDS profiles of the as-deposited FePt/MgO multilayer with X=4.0 nm.

CHAPTER IV

RESULTS

4.1 Magnetic Properties

Figure 4.1 shows the out-of-plane hysteresis loops for the whole series of annealed FePt/MgO multilayers. The magnetic properties, coercivity (H_c) and squareness ratio ($S = M_r/M_s$), as a function of FePt layer thickness are summarized in Table 4.1.

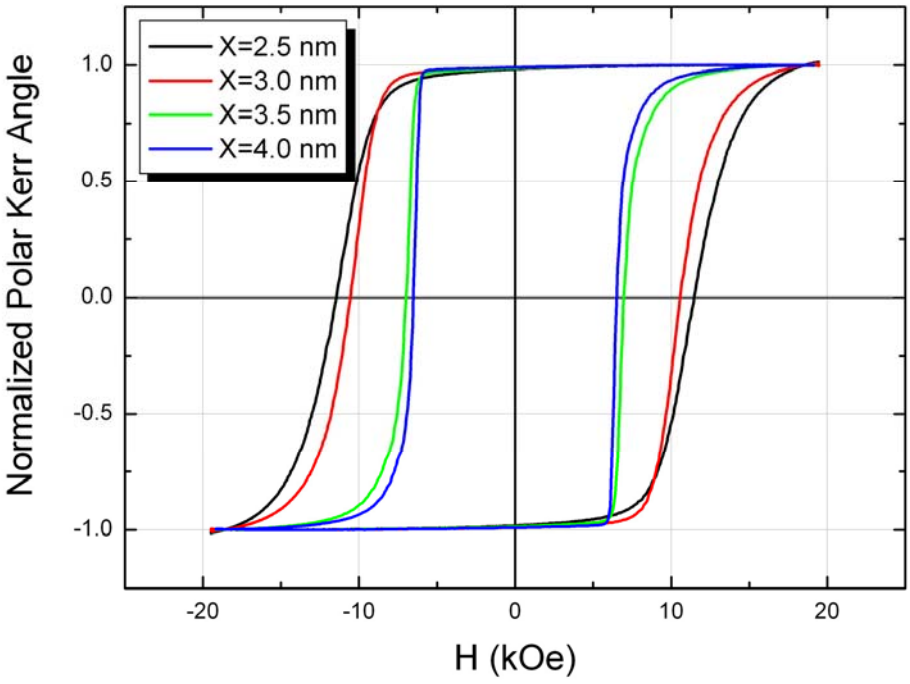

Figure 4.1 Perpendicular hysteresis loops of the annealed FePt/MgO multilayers with X=2.5, 3.0, 3.5, 4.0 nm.

Table 4.1 Magnetic properties of the annealed FePt/MgO multilayers.

FePt layer thickness X (nm)	H_c (kOe)	S (M_r/M_s)
2.5	11.5	0.98
3.0	10.5	0.99
3.5	6.9	0.99
4.0	6.5	0.99

It is found that the squareness ratio S is close to unity for all the annealed FePt/MgO multilayers. This result indicates that perpendicular anisotropy is achieved using the MgO seedlayers and FePt/MgO laminations. However, since S is not unity, the magnetic easy axis (c-axis) is not perfectly perpendicular to the film plane but has a small dispersion around the plane normal. For simple estimation, the dispersion angle of the c-axis can be calculated from $\cos\theta = M_r/M_s$ and thereby θ is found to be around $9^o \sim 10^o$.

All the annealed FePt samples exhibit large coercivities above 6.5 kOe (Figure 4.1 and Table 4.1), which is due to the formation of the highly anisotropic $L1_0$ phase after annealing. However, unlike the squareness ratio which is independent of the FePt layer thickness X, H_c decreases from 11.5 kOe to 6.5 kOe as X increases from 2.5 nm to 4.0 nm. In Figure 4.1, it is also found that the slope of the normalized Kerr angle at coercivity, which is related to the hysteresis loop slope α, increases with increasing FePt layer thickness. Since perpendicular recording media are more exchange coupled at larger values of α [3,38], this reduction in coercivity and increase in α can be attributed to enhanced exchange coupling between the FePt grains. Therefore, the annealed multilayers with thicker FePt layer thickness (X=3.5 and 4.0 nm) may have stronger inter-granular exchange coupling than the multilayers with thinner FePt thickness (X=2.5 and 3.0 nm).

4.2 Microstructure Characterization

4.2.1 EDS Profiles

Figure 4.2 shows the EDS profiles of the FePt/MgO multilayer with X=4.0 nm before and after annealing. Although not quantitative, the x-ray intensity profiles for Mg, Fe, and Pt reveal composition gradients for Fe and Pt in the as-deposited condition (Figure 4.2a), which is consistent with the growth conditions, i.e., the Fe layer and the Pt layer were deposited sequentially. Even though the Fe layer was deposited first, the EDS data show that there is significant inter-mixing of Fe and Pt atoms in the as-deposited condition. However, annealing removed this concentration gradient through interdiffusion of Fe and Pt atoms resulting in homogeneous FePt layers as shown by the EDS profile in Figure. 4.2b. The Fe-Pt composition gradient is also observed in the as-deposited film with X=2.5 nm, but is not as prominent and also disappeared after annealing.

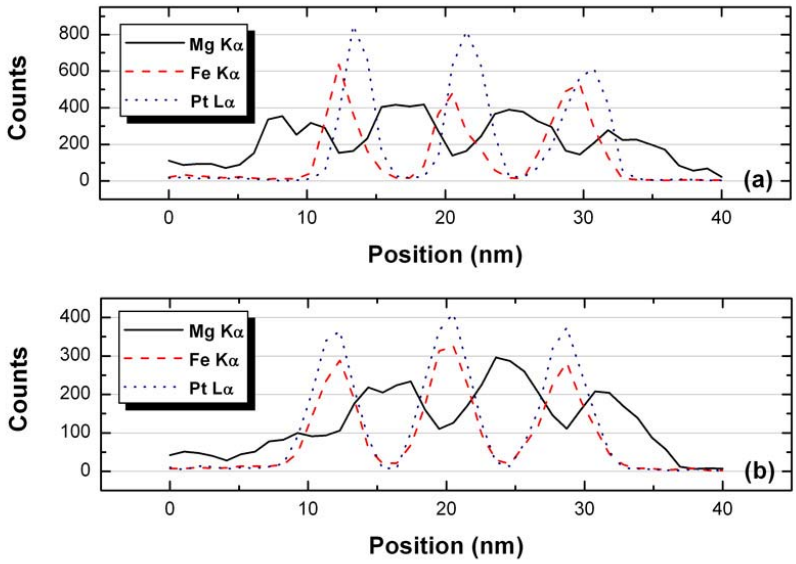

Figure 4.2 EDS profiles of the as-deposited FePt/MgO multilayer with X=4.0 nm along the growth direction (a) before and (b) after annealing.

4.2.1 Electron Diffraction

As-Deposited FePt/MgO multilayer with X=2.5 nm

Figure 4.3 shows SAD patterns of the as-deposited FePt/MgO multilayer with X=2.5 nm. In Figure 4.3a, the electron beam is aligned normal to the film plane (0^o tilt) where (hk0) reflections from the as-deposited polycrystalline FePt grains and MgO grains are observed. These diffraction rings can be indexed as a combination of FCC FePt and cubic MgO without any reflections from body-centered cubic (BCC) iron. When the sample is tilted in the TEM, the diffraction rings change into arcs, as shown in Figure 4.3b, indicating that the as-deposited FePt/MgO multilayer is highly textured. The low intensity of the FePt (111) and (311) reflections is consistent with a strong [001] texture and with only a small fraction of randomly oriented FePt grains within the as-deposited film. Since no $L1_0$ superlattice reflections are observed, the as-deposited FePt is in the disordered FCC condition.

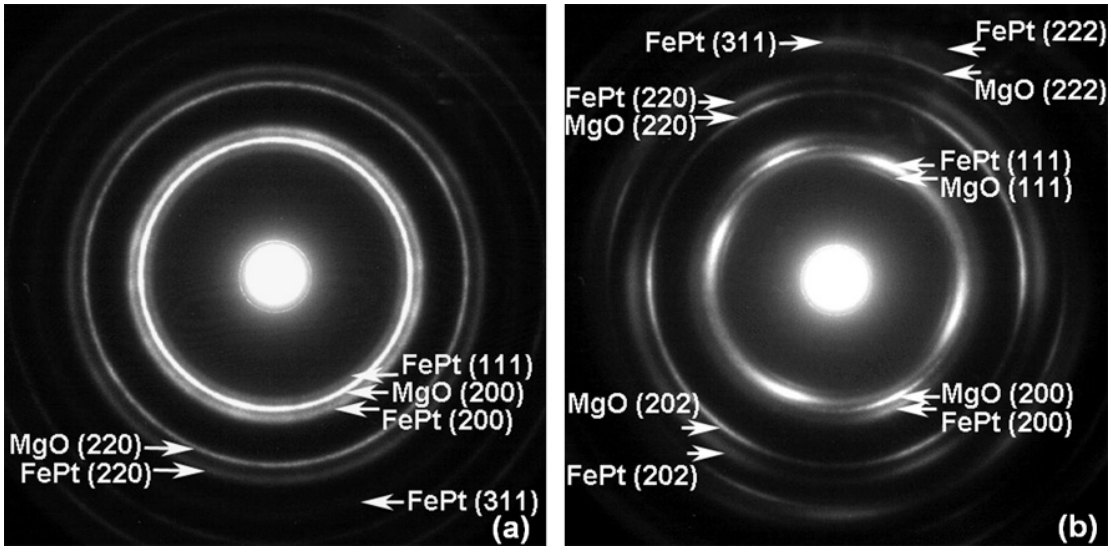

Figure 4.3 SAD patterns of the as-deposited FePt/MgO multilayer with X=2.5 nm. (a) 0^o tilt and (b) 45^o tilt.

As-Deposited FePt/MgO multilayer with X=4.0 nm

Figure 4.4 shows SAD patterns of the as-deposited FePt/MgO multilayer with X=4.0 nm. These two SAD patterns are very similar to those of the as-deposited multilayer with X=2.5 nm shown in Figure 4.3. No superlattice reflections are observed for this sample, which suggests that the FePt is still in the disordered FCC condition, even when the layer thickness is increased to 4.0 nm. The diffraction arcs shown in the SAD pattern from the tilted sample (Figure 4.4b) reveal that this material is also highly textured. The appearance of strong (hk0) reflections together with the weak (111) and (311) reflections in the 0^o tilt pattern (Figure 4.4a) indicates that the as-deposited FePt grains are [001] oriented.

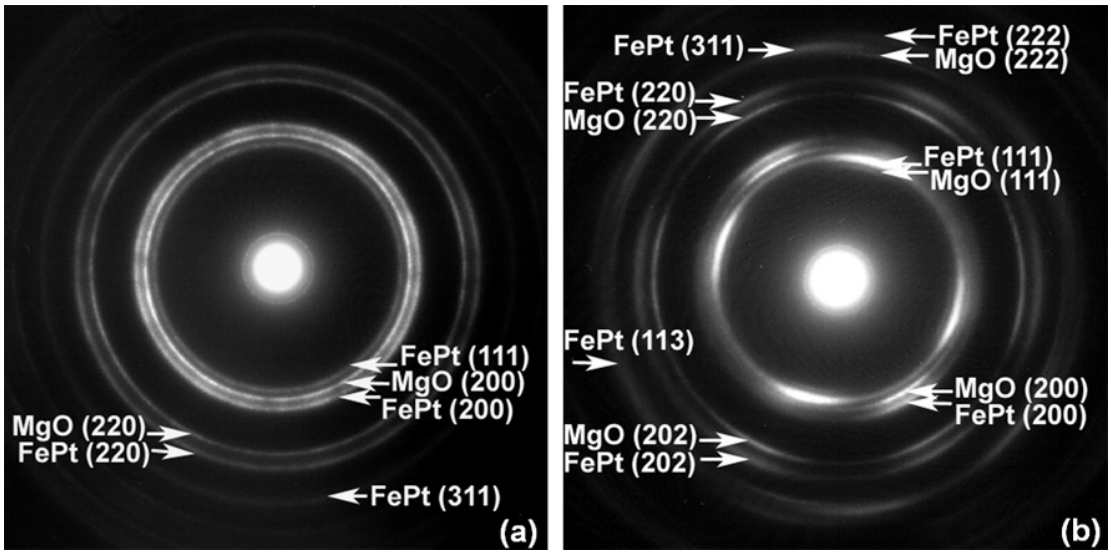

Figure 4.4 SAD patterns of the as-deposited FePt/MgO multilayer with X=4.0 nm. (a) 0^o tilt and (b) 60^o tilt.

Annealed FePt/MgO multilayer with X=2.5 nm

Figure 4.5 shows SAD patterns of the annealed FePt/MgO multilayer with X=2.5 nm. In the annealed condition, (110) and (310) superlattice reflections are present in both 0^o (Figure 4.5a) and 60^o (Figure 4.5b) tilt SAD patterns revealing that the FePt is $L1_0$ ordered with the c-axis normal to the thin film plane. The weak (111) and (311) reflections indicate that the strong [001] texture is retained after annealing. However, annealing does not promote randomly oriented FePt grains to reorient along the [001] direction.

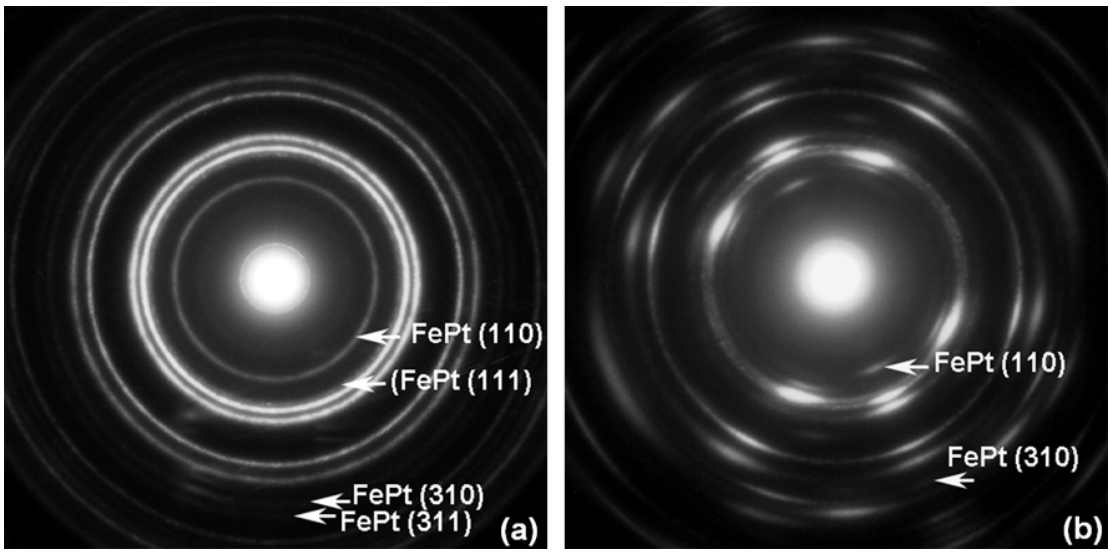

Figure 4.5 SAD patterns of the annealed FePt/MgO multilayer with X=2.5 nm. (a) 0^o tilt and (b) 60^o tilt.

Figure 4.6 shows the plot of $\sin(\omega_{hk0}/2)$ versus $1/\sin\beta$ for the annealed multilayer with X=2.5 nm. The c-axis distribution angle (θ) is determined to be 9^o, which is consistent with S = 0.98 ~ 0.99 ($\cos 9^o = 0.988$). Since the ion-milled thin layers in the plan-view TEM samples have some curvature from the residual stresses in the deposited layers, the actual value of θ is expected to be smaller than the calculated value.

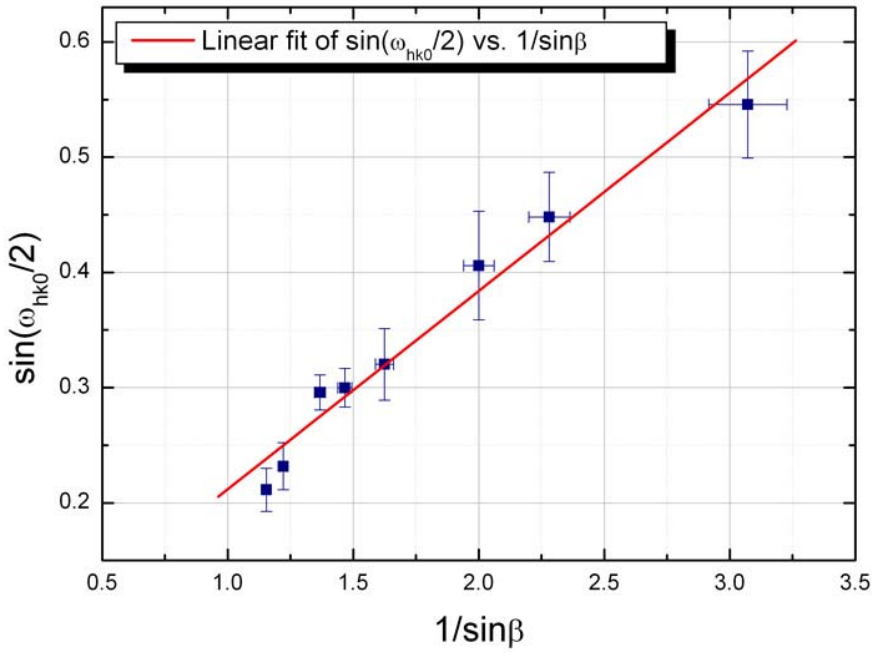

Figure 4.6 The linear regression of $\sin(\omega_{hk0}/2)$ vs. $1/\sin\beta$ from the annealed FePt/MgO multilayer with X=2.5 nm. The c-axis distribution angle is determined to be 9^o.

Annealed FePt/MgO multilayer with X=4.0 nm

Figure 4.7 shows SAD patterns of the annealed FePt/MgO multilayer with X=4.0 nm. These two SAD patterns are similar to those of the annealed multilayer with X=2.5 nm shown in Figure 4.5. Again, (110) and (310) superlattice reflections indicate the presence of the $L1_0$ phase. As can be seen, this annealed film is still not perfectly [001] textured since the weak (111) and (311) reflections are still present in the SAD patterns.

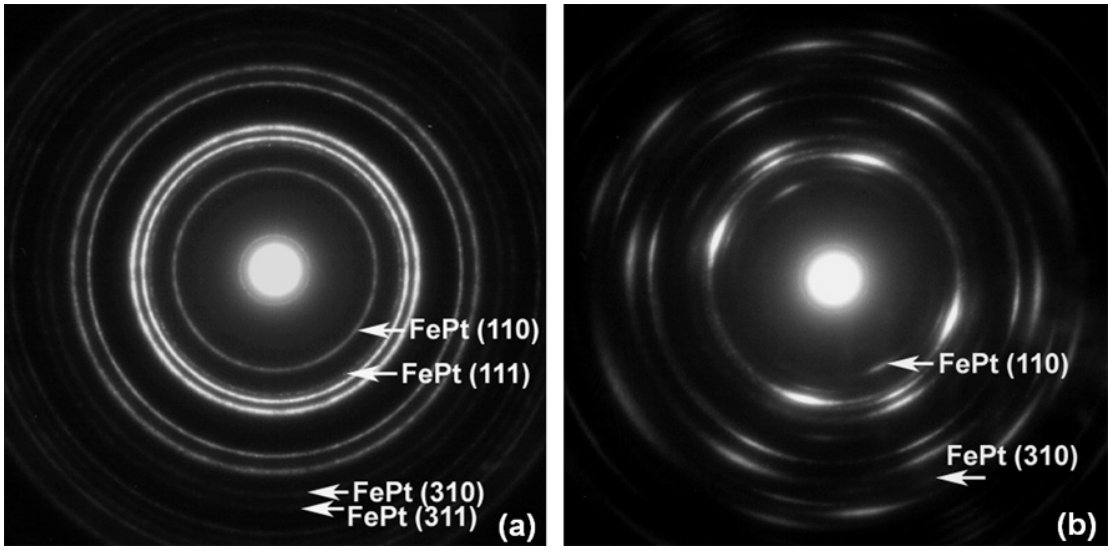

Figure 4.7 SAD patterns of the annealed FePt/MgO multilayer with X=4.0 nm. (a) 0^o tilt, (b) 62^o tilt.

Figure 4.8 shows the plot of $\sin(\omega_{hk0}/2)$ versus $1/\sin\beta$ for the annealed multilayer with X=4.0 nm. The c-axis distribution angle θ is found to be 10^{o}, which is also consistent with S = 0.98 ~ 0.99 ($\cos 10^{o}$ = 0.985). In a similar way to the annealed multilayer with X=2.5 nm, the actual value of θ is expected to be smaller than the calculated value due to the curvature of the electron-transparent regions from the residual stresses within the multilayer.

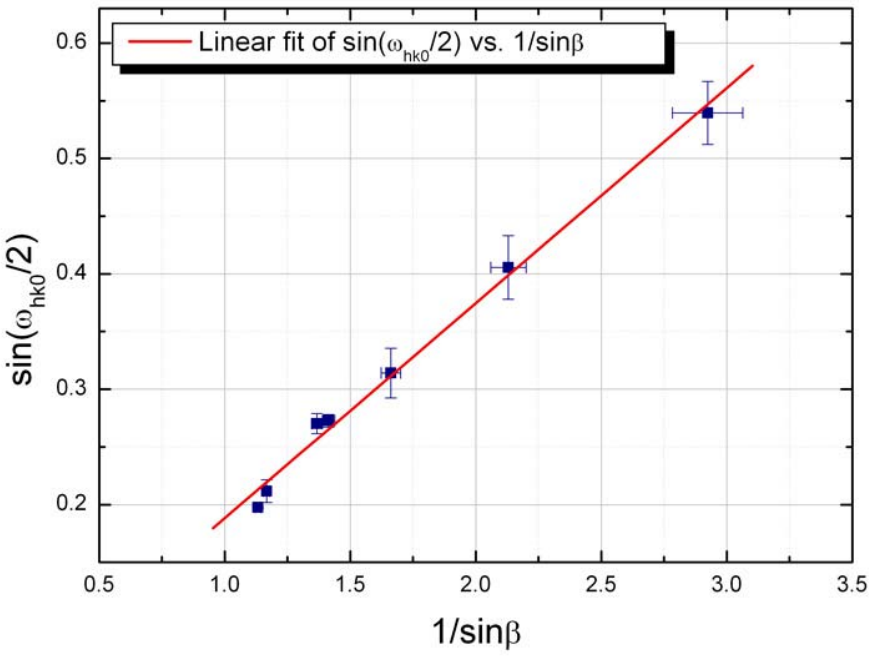

Figure 4.8 The linear regression of $\sin(\omega_{hk0}/2)$ vs. $1/\sin\beta$ from the annealed FePt/MgO multilayer with X=4.0 nm. The c-axis distribution angle is determined to be 10^{o}.

4.2.2 Plan-View HRTEM images

Annealed FePt/MgO multilayer with X=2.5 nm

Figure 4.9 shows plan-view HRTEM images of the annealed FePt/MgO multilayer with X=2.5 nm. In the thin area of this plan-view sample (Figure 4.9a), a layered microstructure is observed. This layered microstructure is consistent with the FePt/MgO laminated structure within the film. Since the plan-view multilayered sample contains many overlapping features, it is very difficult to distinguish the individual FePt grains. The inset in Figure 4.9a shows lattice fringes corresponding to the four-fold symmetry of the cubic MgO and the $L1_0$-structured FePt. These fringes are also observed in the thicker area where strong moiré fringes are present, as shown in Figure 4.9b.

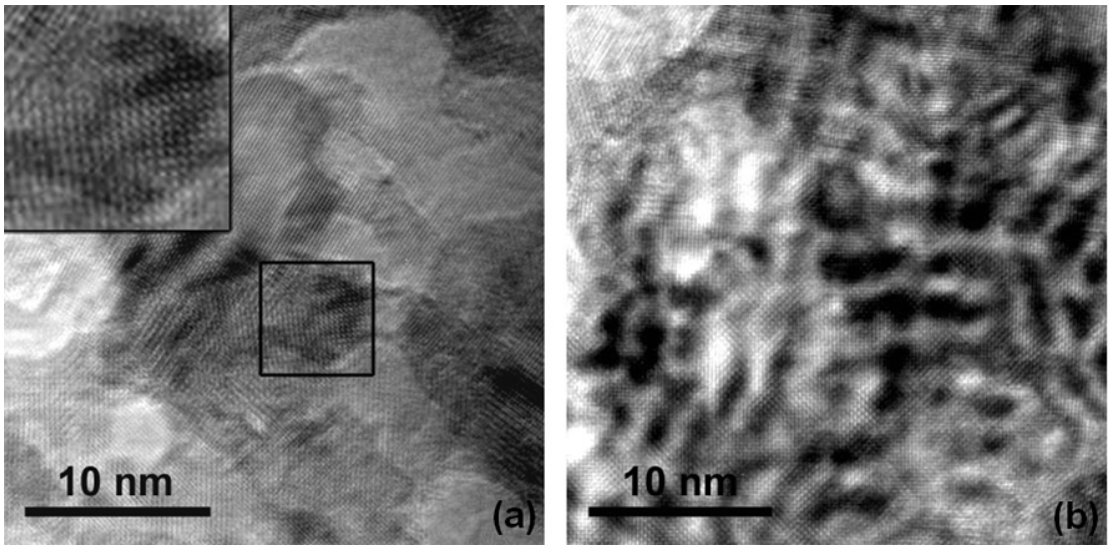

Figure 4.9 Plan-view HRTEM images of the annealed FePt/MgO multilayer with X=2.5 nm. (a) thin area and (b) thick area.

Annealed FePt/MgO multilayer with X=4.0 nm

Figure 4.10 shows plan-view HRTEM images of the annealed FePt/MgO multilayer with X=4.0 nm. These two images are similar to those of the annealed multilayer with X=2.5 nm. Consistent with a [001] textured FePt/MgO multilayer, the lattice fringes from the cubic MgO and the $L1_0$-structured FePt are present in both thin (Figure 4.10a) and thick (Figure 4.10b) areas.

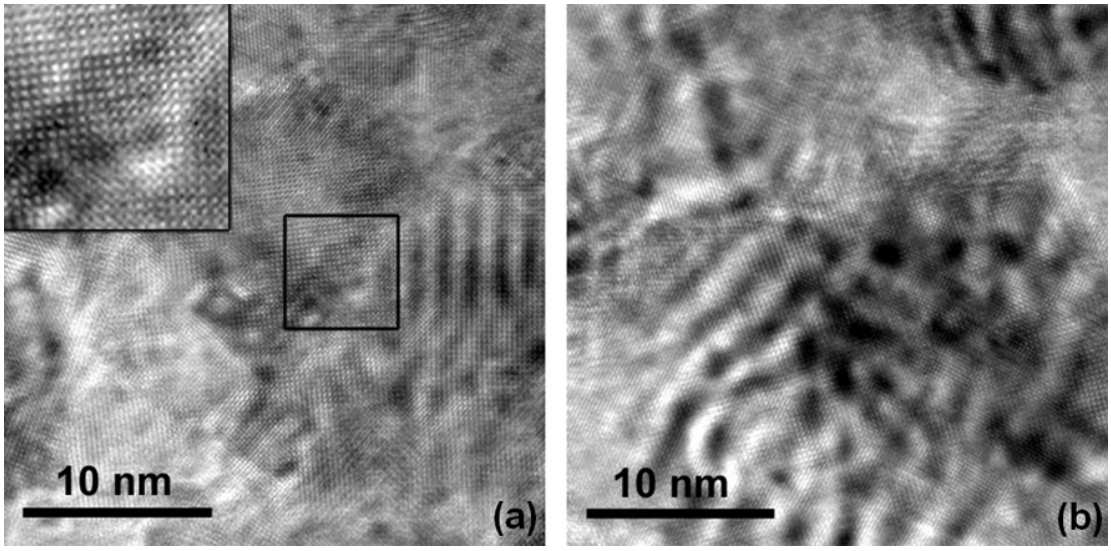

Figure 4.10 Plan-view HRTEM images of the annealed FePt/MgO multilayer with X=4.0 nm. (a) thin area and (b) thick area.

4.2.3 Cross-Sectional BF and HRTEM images

FePt/MgO multilayer with X=2.5 nm

Figure 4.11 shows cross-sectional view BF images of the FePt/MgO multilayer with X=2.5 nm before and after annealing. In the as-deposited condition, all the FePt layers are continuous as shown in the inset. However, the continuous FePt layers became discontinuous after annealing. As can be seen, within a single layer the FePt regions are separated by MgO, and the spacing between these regions ranges from a few nm to 25 nm. A possible explanation of the continuity change of the FePt layers is that during annealing, the FePt layers tend to break up themselves to minimize interfacial energy. Consequently, holes are formed in the FePt layers, and MgO diffuse into theses holes forming “island-like” structure.

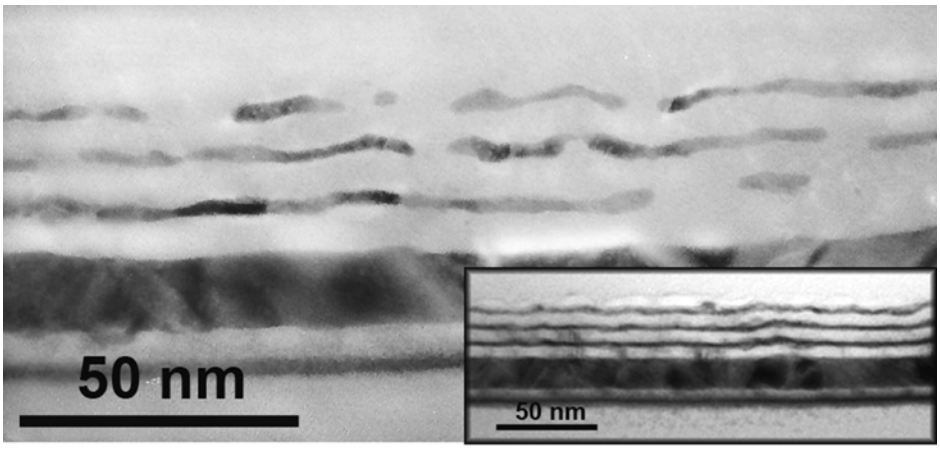

Figure 4.11 Cross-sectional view BF images of the FePt/MgO multilayer with X=2.5 nm before (inset) and after annealing.

Figure 4.12 shows cross-sectional view HRTEM images of this sample in the as-deposited and annealed conditions. The lattice fringes showing the stacking of layers of atoms are clearly observed in both the FePt and the MgO layers. In the annealed condition (Figure 4.12b), the white-gray region in the discontinuous FePt layer reveals that there is MgO diffused into this region of the FePt layer.

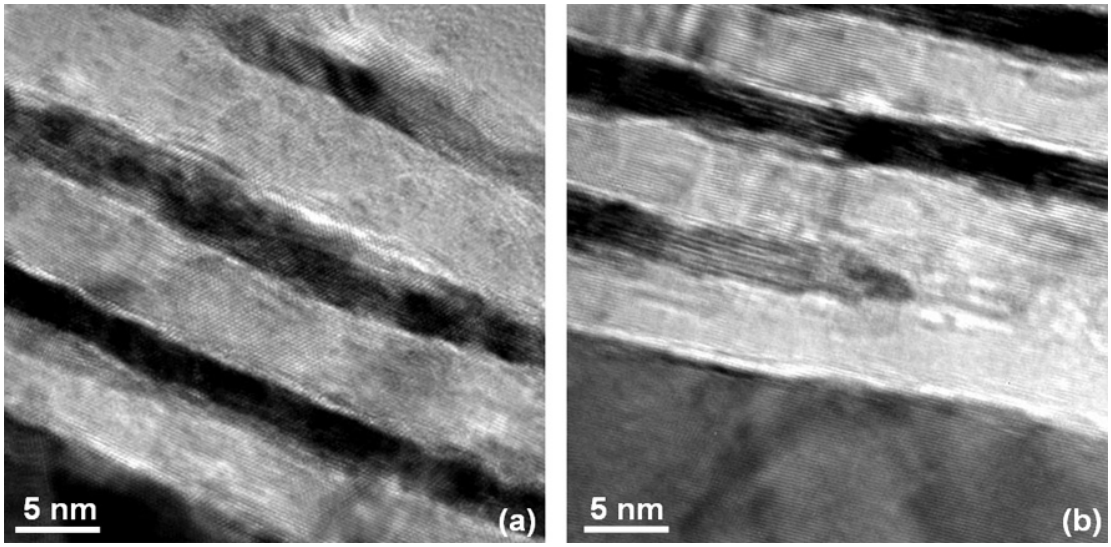

Figure 4.12 Cross-sectional view HRTEM images of the FePt/MgO multilayer with X=2.5 nm in (a) as-deposited and (b) annealed conditions.

FePt/MgO multilayer with X=4.0 nm

Figure 4.13 shows cross-sectional view BF images of the FePt/MgO multilayer with X=4.0 nm before and after annealing. Unlike the multilayer with X=2.5 nm, all the FePt layers in this sample remained continuous after annealing. Since the FePt layers are thicker in this sample, the interfacial energy minimization effect is not so appreciable, i.e., the annealed FePt did not break up forming the "island-like" microstructure as shown in the cross-sectional view sample with X=2.5 nm.

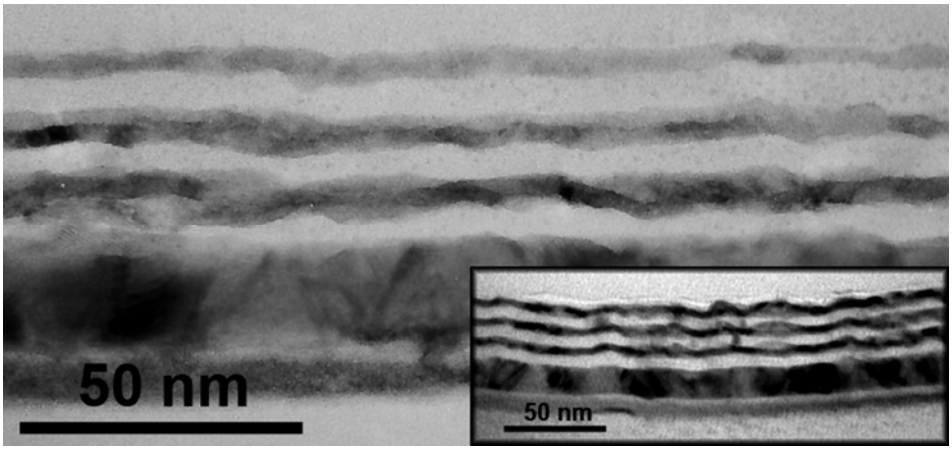

Figure 4.13 Cross-sectional view BF images of the FePt/MgO multilayer with X=4.0 nm before (inset) and after annealing.

Figure 4.14 shows cross-sectional view HRTEM images of this sample in the as-deposited and annealed conditions. In a similar way to the multilayer with X=2.5 nm, the lattice fringes showing the stacking of layers of atoms are also observed in this sample.

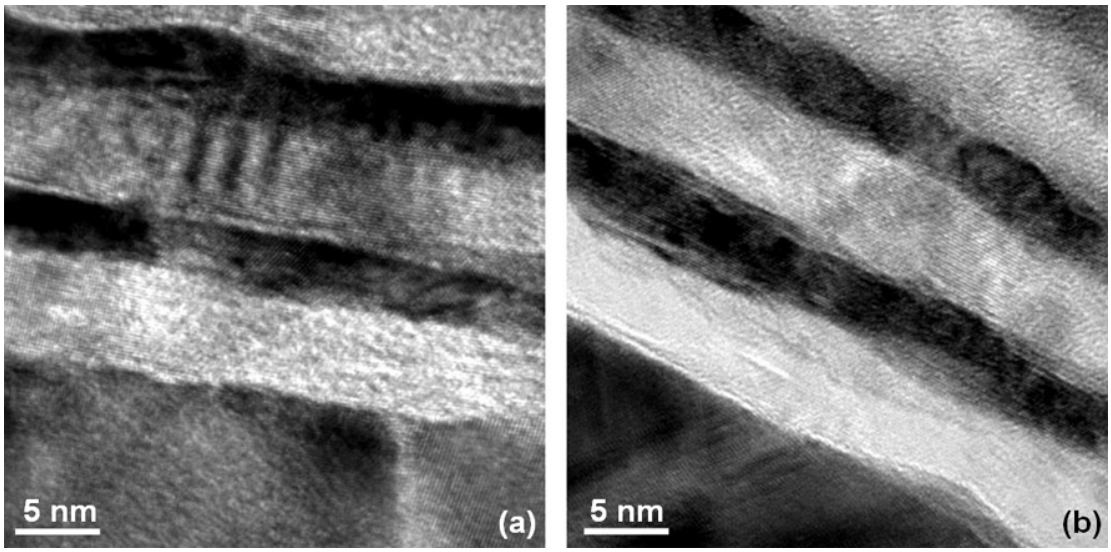

Figure 4.14 Cross-sectional view HRTEM images of the FePt/MgO multilayer with X=4.0 nm in (a) as-deposited and (b) annealed conditions.

4.2.4 Cross-Sectional EFTEM Images

As-Deposited FePt/MgO multilayer with X=2.5 nm

Figure 4.15 shows cross-sectional view EFTEM images of the as-deposited FePt/MgO multilayer with X=2.5 nm. The Fe map (Figure 4.15a) and jump-ratio (Figure 4.15c) images reveal that the FePt layers are continuous in the as-deposited condition. The continuity of the FePt layers is also observed in the O map (Figure 4.15b) and jump-ratio (Figure 4.15d) images where the FePt layers are present as the dark layers between the brightly imaging MgO layers.

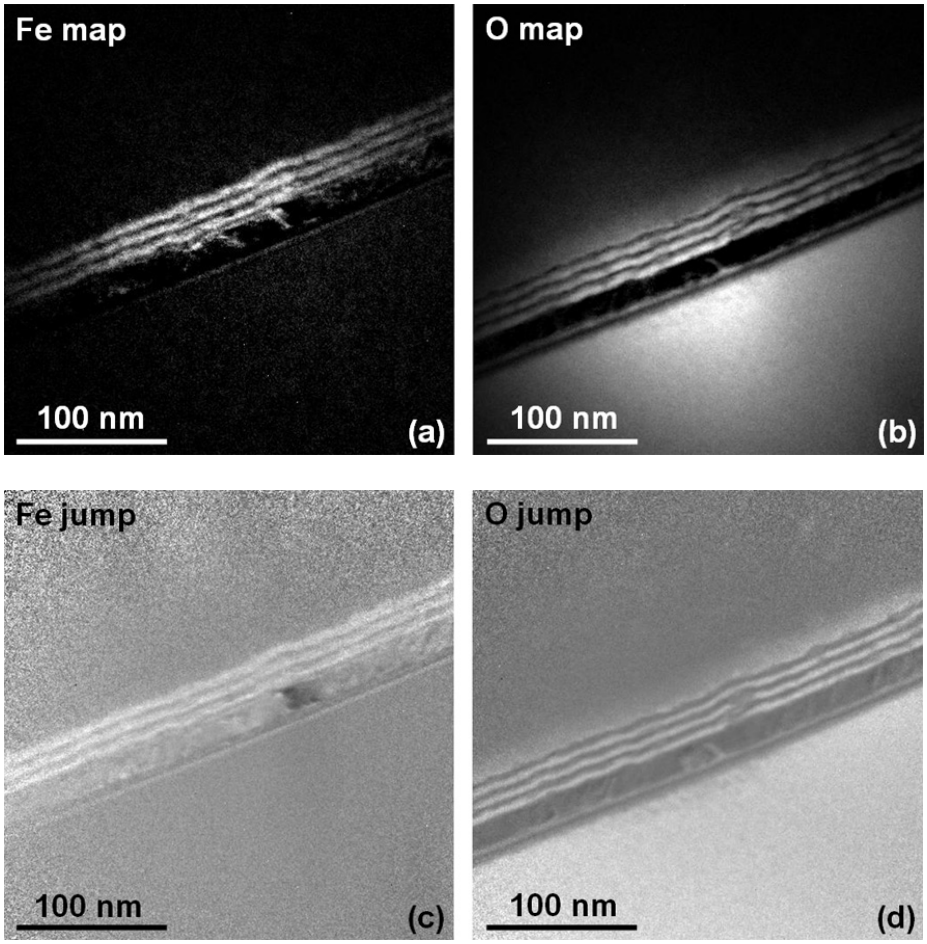

Figure 4.15 Cross-sectional view EFTEM images of the as-deposited FePt/MgO multilayer with X=2.5 nm. (a) Fe map, (b) O map, (c) Fe jump-ratio and (d) O jump-ratio.

Annealed FePt/MgO multilayer with X=2.5 nm

Figure 4.16 shows cross-sectional view EFTEM images of the annealed FePt/MgO multilayer with X=2.5 nm. Both the Fe and O maps (Figure 4.16a and 4.16b) show that the FePt layers are discontinuous after annealing. The discontinuous FePt layers are also clearly shown in the jump-ratio images (Figure 4.16c and 4.16b) where the influences of diffraction contrast and variation in sample thickness are reduced.

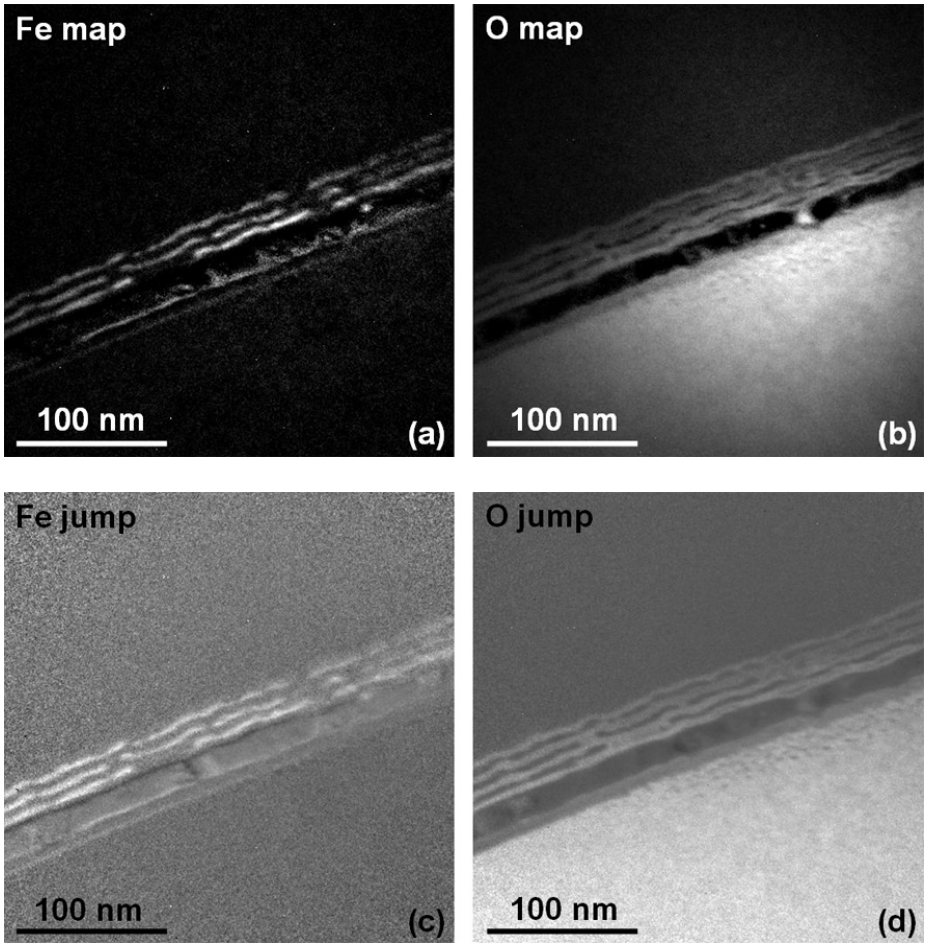

Figure 4.16 Cross-sectional view EFTEM images of the annealed FePt/MgO multilayer with X=2.5 nm. (a) Fe map, (b) O map, (c) Fe jump-ratio and (d) O jump-ratio.

As-Deposited FePt/MgO multilayer with X=4.0

Figure 4.17 shows cross-sectional view EFTEM images of the as-deposited FePt/MgO multilayer with X=4.0 nm. As can be seen, these EFTEM images reveal that the FePt layers in this sample are continuous in the as-deposited condition.

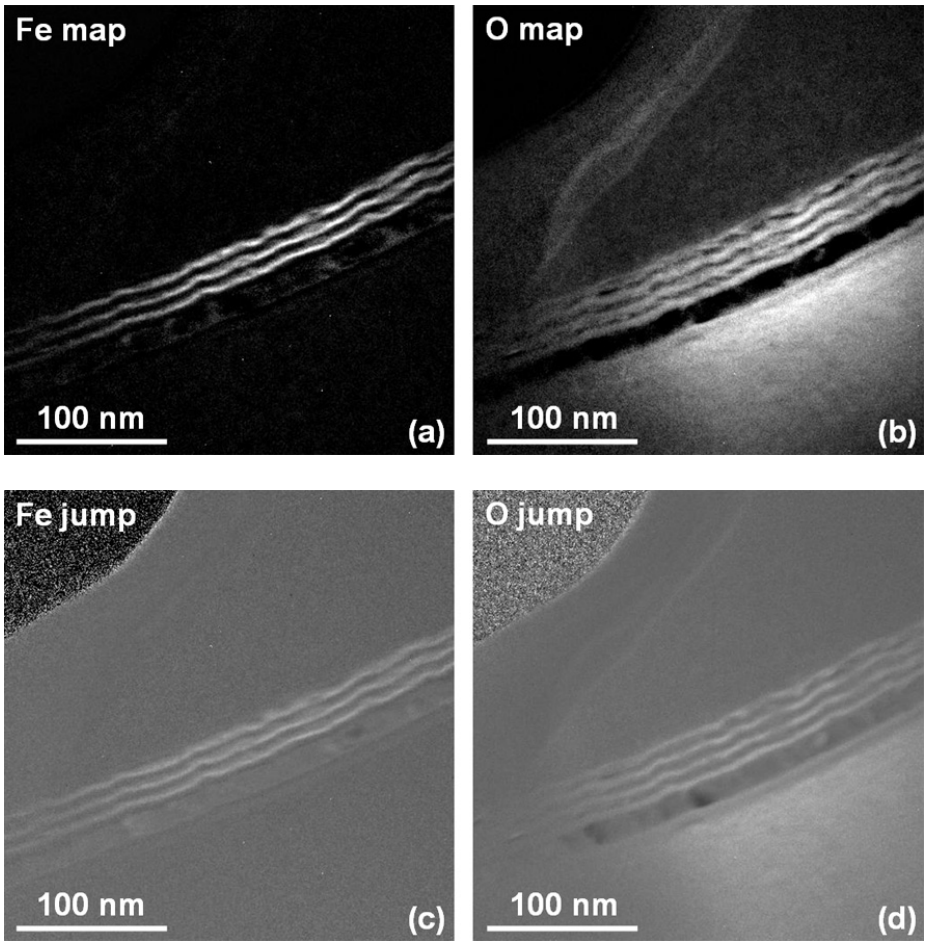

Figure 4.17 Cross-sectional view EFTEM images of the as-deposited FePt/MgO multilayer with X=4.0 nm. (a) Fe map, (b) O map, (c) Fe jump-ratio and (d) O jump-ratio.

Annealed FePt/MgO multilayer with X=4.0 nm

Figure 4.18 shows cross-sectional view EFTEM images of the annealed FePt/MgO multilayer with X=4.0 nm. Consistent with the results shown in the cross-sectional view images in Figure 4.13 and 4.14, the FePt layers are seen to remain continuous after annealing. No broken "island" microstructure is observed in this sample.

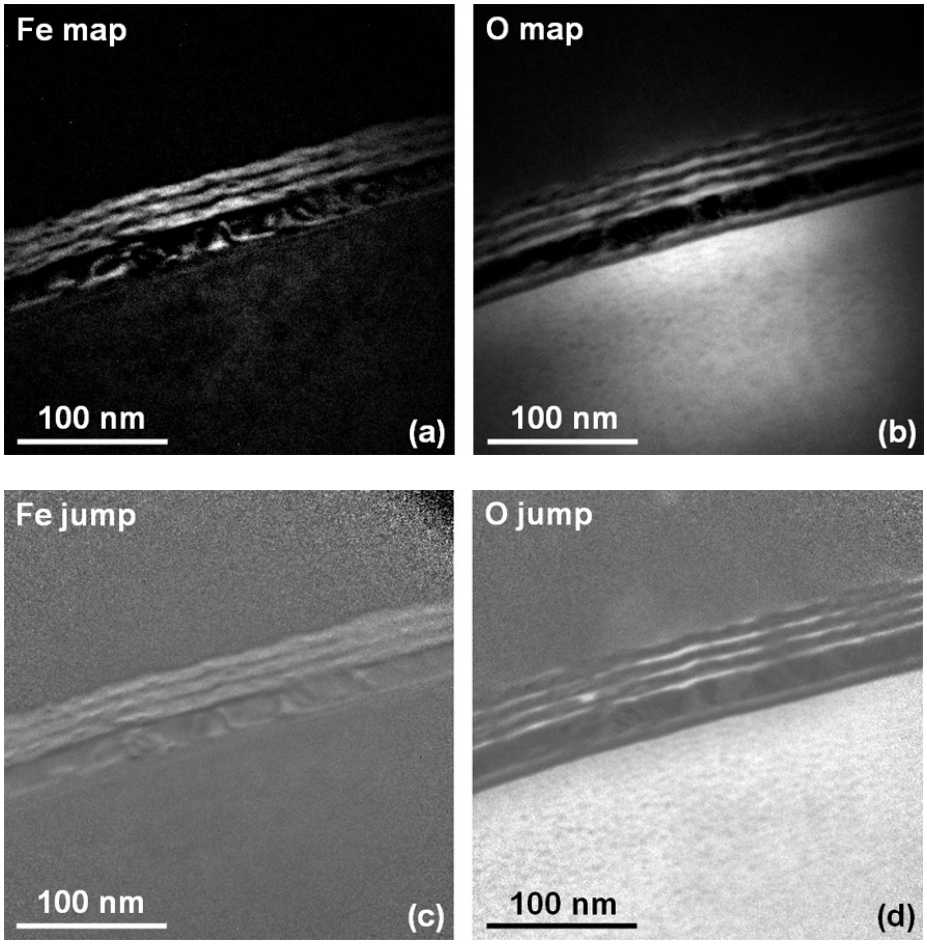

Figure 4.18 Cross-sectional view EFTEM images of the annealed FePt/MgO multilayer with X=4.0 nm. (a) Fe map, (b) O map, (c) Fe jump-ratio and (d) O jump-ratio.

4.2.5 Plan-View EFTEM Images

Annealed FePt/MgO multilayer with X=2.5 nm

Figure 4.19 shows plan-view EFTEM images of the annealed FePt/MgO multilayer with X=2.5 nm. Unlike the plan-view HRTEM images, these EFTEM images clearly unveil the actual microstructure within the film. The Fe elemental map (Figure 4.19a) reveals the regions without Fe, i.e., the dark regions. This discontinuous distribution of FePt is perhaps more clearly observed in the jump-ratio image (Figure 4.19c). The size of the dark regions in Figures 4.19a and 4.19c ranges from a few nm to 30 nm, which is consistent with the gap spacing between the FePt "islands" observed in the cross-sectional sample shown in Figure 4.11.

Annealed FePt/MgO multilayer with X=4.0 nm

Figure 4.20 shows plan-view EFTEM images of the annealed FePt/MgO multilayer with X=4.0 nm. The Fe map (Figure 4.20a) and jump-ratio (Figure 4.20b) images show only a few regions with no Fe. Therefore, the FePt layers in this sample are more continuous as compared to the annealed multilayer with X=2.5 nm.

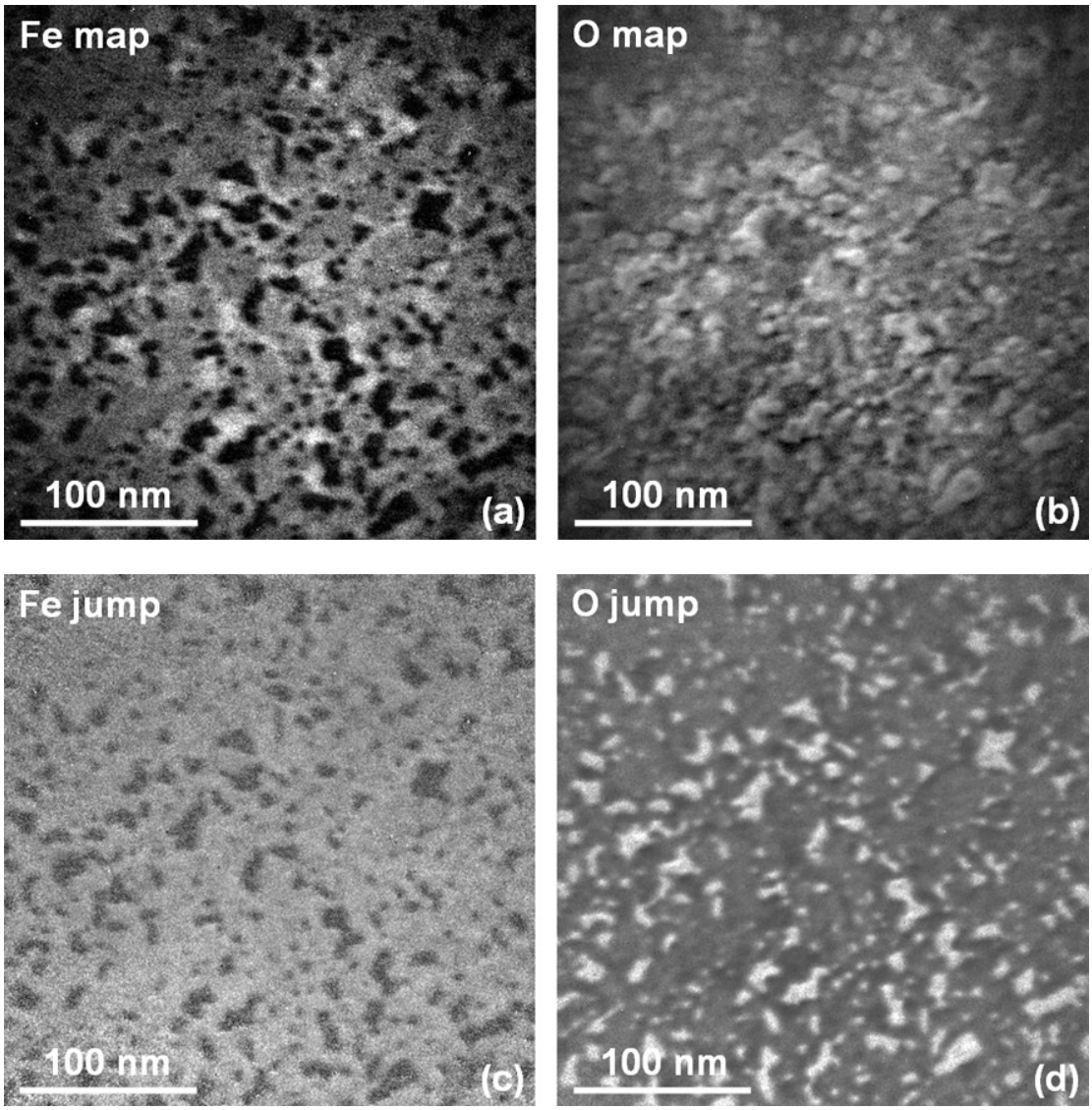

Figure 4.19 Plan-view EFTEM images of the annealed FePt/MgO multilayer with X=2.5 nm. (a) Fe map, (b) O map, (c) Fe jump-ratio and (d) O jump-ratio.

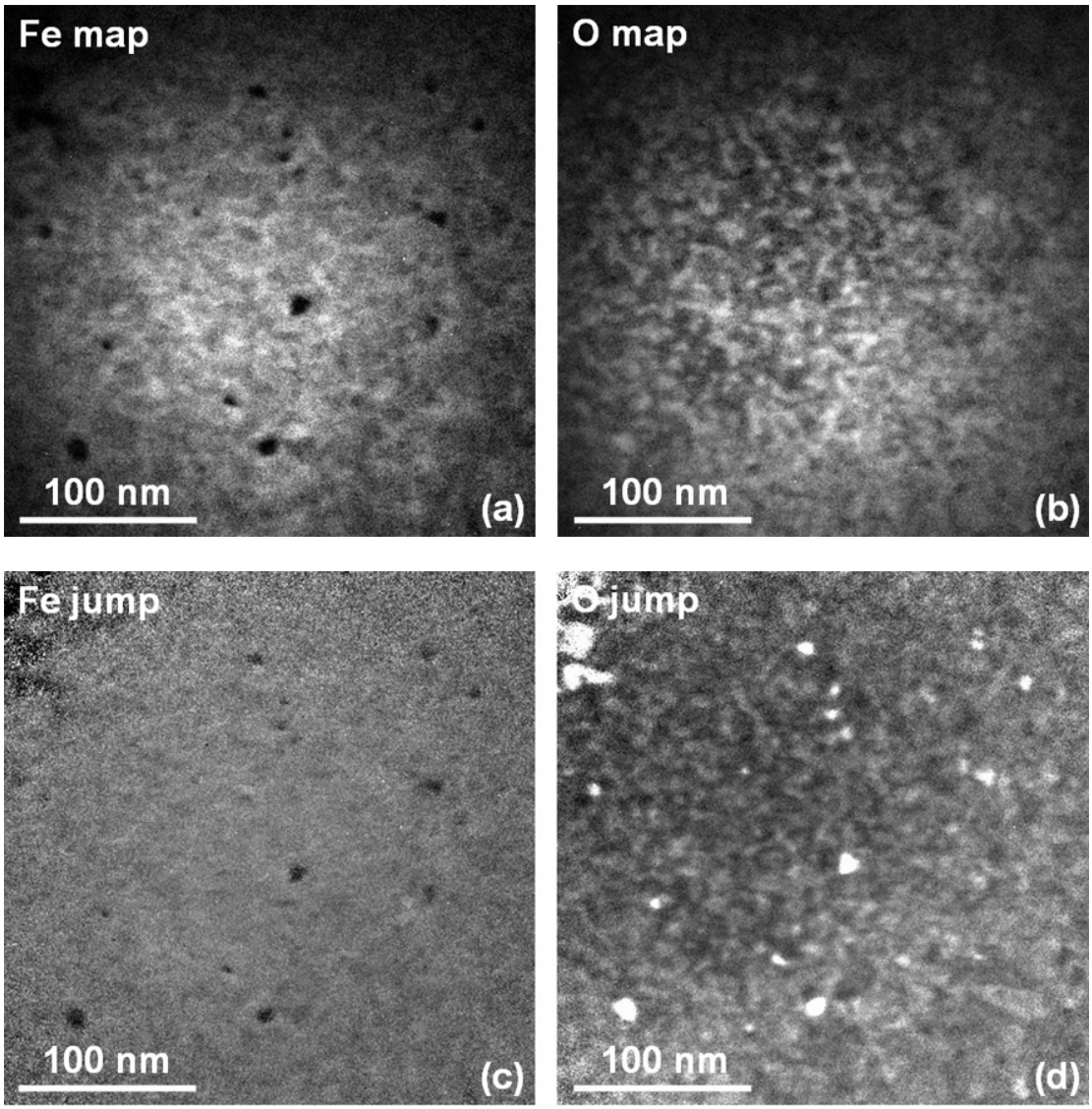

Figure 4.20 Plan-view EFTEM images of the annealed FePt/MgO multilayer with X=4.0 nm. (a) Fe map, (b) O map, (c) Fe jump-ratio and (d) O jump-ratio.

CHAPTER V

DISCUSSION

5.1 MgO Seedlayers

In this research, MgO was selected as the seedlayers for heteroepitaxial growth of the FePt thin films. This is because the sputter deposited MgO has a cubic structure with a similar lattice spacing to that of FCC FePt and can develop a strong [001] texture even on an amorphous substrate. Therefore, [001] textured FePt can be easily induced by heteroepitaxially growing FePt thin films on the [001] oriented MgO seedlayers.

In the electron diffraction studies, the diffraction arcs shown in the SAD patterns from tilted samples (Figure 4.3b and 4.4b) indicate that the as-deposited MgO seedlayers are highly textured. Since MgO has only the (hk0) reflections present in the 0^o tilt SAD patterns (Figure 4.3a and 4.4a), the strong texture established in the seedlayers is confirmed to be the [001] texture. These SAD patterns shown in Figure 4.3 and 4.4 also reveal that the as-deposited FePt layers are highly [001] textured. However, the presence of the weak FePt (111) and (311) reflections suggests that there is a small fraction of randomly oriented FePt grains within the as-deposited films. Since the lattice misfit of the cubic MgO and FCC FePt is 9.5%, the presence of the mis-oriented FePt grains can be attributed to the interfacial stresses induced by the heteroexpitaxial film growth.

5.2 MgO/FePt Laminated Structure

In the hard disk drive, the magnetic recording media must have a certain layer thickness to maintain a high enough magnetic flux for data storage. However, it is usually

difficult to grow a thick FePt film while keeping a strong [001] texture [30,34]. Therefore, instead of growing a single thick FePt layer, a MgO/FePt laminated structure was employed in this research to prepare the thin films.

The SAD patterns shown in Figure 4.3 and 4.4 reveal that the as-deposited FePt layers are highly [001] textured. Even when the FePt layer thickness is increased from 2.5 nm to 4.0 nm, no apparent degradation of the [001] texture is observed. Since each FePt layer is grown between two strongly [001] textured MgO layers, the probability of texture degradation during post-deposition annealing is largely reduced. Therefore, the strong [001] texture developed in the as-deposited FePt/MgO multilayers is successfully preserved after annealing by using the laminated structure (Figure 4.5 and 4.7).

The second advantage of employing MgO laminations is that they can assist the ordering of FePt grains along the [001] direction during post-deposition annealing. Figure 2.8 shows the lattice distortion associated with chemical ordering during phase transformation. For the as-deposited FCC FePt grains, the lattice parameter is 3.816 Å. After annealing, the FePt grains transform from the disordered FCC phase to the ordered FCT phase by alternate stacking of planes of pure Fe atoms and pure Pt atoms along the c-axis direction. As a result, the unit-cell size along the c-axis is shortened to 3.713 Å while along the a- and b-axis it is elongated to 3.853 Å. However, the unconstrained FCC FePt lattice has the same probability to order along the [100], [010], and [001] directions during post-deposition annealing, which would result in no perpendicular magnetic anisotropy. Therefore, restrictions must be applied to prevent $L1_0$ ordering along the [100] and [010] directions. When MgO laminations are employed to prepare the FePt thin films, each FePt layer is grown between two MgO layers. Since the lattice misfit of the cubic

MgO and the FCC FePt is 9.5%, the FePt lattice will tend to elongate in the film plane during phase transformation in order to reduce the misfit and residual stresses at the interfaces. Therefore, the probability of $L1_0$ ordering along the [100] and [010] directions is largely reduced. As shown in Figure 4.5 and 4.7, no apparent (100) or (010) reflections are present in the SAD patterns of the annealed FePt/MgO multilayers. Therefore, most of the FePt grains are chemically ordered with the magnetic easy axis perpendicular to the film plane.

5.3 Post-Deposition Annealing

It is known that the as-deposited FePt is disordered FCC phase with no magnetocrystalling anisotropy. To transform FePt from the disordered FCC phase to the ordered FCT phase, high temperature annealing (> 500^{o}C) is usually required [26].

In this research, electron diffraction studies have shown that the as-deposited FePt is in the disordered FCC condition (Figure 4.3 and 4.4). After annealing at 700^{o}C for 30 minutes, (110) and (310) superlattice reflections are present in the SAD patterns shown in Figure 4.5 and 4.7, indicating the formation of the $L1_0$-ordered phase. In the magnetic property measurements, high coercivities (> 6.5 kOe) are observed for all the annealed FePt/MgO multilayers, revealing that the FePt is in the $L1_0$-ordered phase after annealing. Therefore, annealing at 700^{o}C for 30 minutes successfully transform the FePt layers from the disordered FCC phase into the $L1_0$-ordered phase. However, it is found that post-deposition annealing does not promote randomly oriented FePt grains in the as-deposited film to be reoriented along the [001] direction. These misoriented FePt

grains may be partially responsible for the dispersion of the average c-axis orientation which will be discussed in the next section.

5.4 Average Orientation of the Magnetic Easy Axis

Unlike longitudinal media where the grains are magnetized in the film plane, the magnetic easy axis of perpendicular media needs to be aligned normal to the film plane in order to facilitate perpendicular recording. For the $L1_0$-ordered FePt, the magnetic easy axis is the c-axis. Therefore, the quality of the c-axis orientation can have a strong influence on the magnetic properties of FePt recording media.

In the electron diffraction studies, the SAD patterns show that the annealed FePt/MgO multilayers are highly [001] textured (Figure 4.5 and 4.7). The average c-axis orientation, which is quantified as the distribution angle (θ), is determined to be ~ 10^o for the annealed multilayers (Figure 4.6 and 4.8). The small dispersion of the c-axis indicates that the magnetic easy axes of these annealed multilayers are not perfectly perpendicular to the film plane but distributed within a ~ 10^o solid angle around the plane normal. It is known that in spontaneous magnetization, the magnetic moments always prefer to line up with the magnetic easy axis. Therefore, the out-of-plane component of the magnetization vector, which is the remanent magnetization (M_r) shown in the perpendicular hysteresis loop, is equal to the product of the saturation magnetization (M_s) and the cosine of the distribution angle (θ), i.e. $M_r = M_s\cos\theta$. Since the squareness ratio is defined as $S = M_r/M_s$, it is easy to estimate $S = 0.985$ ($\cos 10^o = 0.985$). This result is consistent with the high squareness ratios obtained in the magnetic property measurements, where S is found to be 0.98 ~ 0.99 and to be independent of the FePt layer thicknesses.

5.5 Grain Size

For magnetic recording, the read-back SNR is inversely proportional the third power of the magnetic grain size [19]. Therefore, recording media with small grain size and narrow grain size distribution can effectively increase the SNR. However, FePt grains tend to coarsen into large particles during annealing [35]. Figure 5.1 shows a plan-view BF image of a single layered FePt thin film annealed at 750^{o}C for 10 minutes. Although the FePt was co-sputtered with MgO during deposition, the FePt grains still coarsened into very large particles (> 100 nm in diameter) after annealing. Therefore, employing a new method to inhibit FePt grain coarsening during annealing is important for preparation of FePt recording media.

In this research, MgO laminations were used to prepare the FePt magnetic thin films. It is found that grain growth in the out-of-plane direction is inhibited by this laminated structure. As shown in cross-sectional BF images of the annealed FePt/MgO multilayers (Figure 4.11 and Figure 4.13), although the roughness of the FePt layers is increased due to grain growth, no large particles are formed in the direction perpendicular to the film plane. Since each FePt layer is grown between two MgO layers, FePt grain coarsening in this direction is inhibited by the limited spacing between the adjacent MgO layers. In the film plane, however, there is no restriction to inhibit FePt grain growth. It is still possible that the FePt grains can coarsen into large particles. Unfortunately, the overlapping features in the plan-view TEM samples (Figure 4.9 and 4.10) make the direct measurement of grain size very difficult. Therefore, to measure the in-plane FePt grain size, it is necessary to employ dark-field (DF) imaging to investigate plan-view samples which have only one FePt layer grown between two MgO layers.

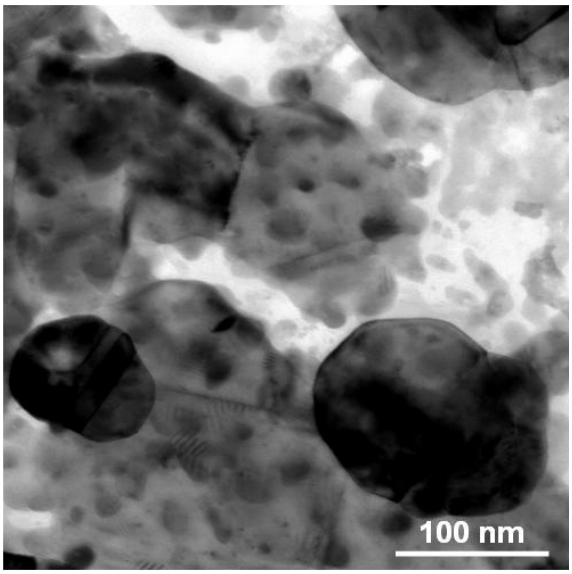

Figure 5.1 Plan-view BF image of an annealed single layered FePt film (co-deposited with MgO). The FePt grains coarsened into large particles after annealing at 750^{o}C for 10 minutes. (This sample was prepared by Seagate Technology.)

5.6 Grain Separation

It is known that exchange coupling between the magnetic grains of recording media is largely responsible for media noise [39,40,41]. Theoretical and experimental results show that inter-granular coupling can cause the grains to form large magnetic clusters where all the grains inside this cluster have the same magnetization direction. These magnetic clusters are usually much larger than the individual crystalline grains. Consequently, the zigzag shape of the transition region between two oppositely recorded bits becomes more pronounced (larger amplitude of deviations from a sharp linear transition) and results in a timing jitter-induced noise [42]. Therefore, the key to reduce media noise for high-density magnetic recording is to minimize the strong exchange interactions between magnetic grains. Since exchange coupling arises from short range interactions which usually decrease exponentially with grain separation, large efforts

have been given to prepare granular media where the magnetic grains are well separated by nonmagnetic material at the grain boundaries [42].

In this research, MgO laminations were intentionally used to assist FePt recording layers to develop a strong [001] texture. It was also anticipated that during annealing MgO would diffuse along the FePt grain boundaries so that each individual FePt grain would be separated by MgO. However, a granular microstructure is not observed in the annealed FePt/MgO multilayers. For the multilayer with X=4.0 nm, the FePt layers tend to be continuous after annealing. The continuous distribution of Fe atoms shown in the plan-view Fe map and jump-ratio images (Figure 4.20) indicates that MgO does not appreciably diffuse into the FePt layers during annealing. A possible explanation is that grain boundaries in the continuous FePt layers do not provide diffusion paths for MgO. Therefore, no granular microstructure is formed and thereby the FePt grains are strongly exchange coupled within this sample. When the FePt layer thickness is reduced to 2.5 nm, the FePt layers become discontinuous after annealing due to the interfacial energy minimization effect. The plan-view EFTEM images (Figure 4.19) reveal that there are many regions where there is no Fe. The size of these regions ranges from a few nm to 30 nm and is consistent with the gap spacing between the FePt “islands” observed in the cross-sectional BF (Figure 4.11) and EFTEM images (Figure 4.16). Since MgO diffuses into these regions which have no Fe, exchange coupling between the FePt grains is partially reduced. However, it must be noticed that there is still a large portion of the FePt layers that remained continuous in this sample, as shown in Figure 4.19. Therefore, using MgO laminations is unable to effectively separate the FePt grains, even if the FePt layer thickness is reduced to 2.5 nm.

5.7 FePt Layer Continuity and Magnetic Properties

In the magnetic property measurements (Section 4.1), it is shown that the magnetic properties of the annealed FePt/MgO multilayers change with the FePt layer thickness. The multilayer with X=2.5 nm exhibits the largest coercivity and smallest hysteresis loop slope among all the annealed multilayers. As the FePt layer thickness is increased from 2.5 nm to 4.0 nm, H_c decreases from 11.5kOe to 6.5 kOe. Meanwhile, it is also found that the hysteresis loop slope increases as the FePt layer thickness becomes thicker. Since perpendicular recording media with large loop slopes are more exchange coupled [3,38], the reduction in coercivity and the increase in hysteresis loop slope can be attributed to enhanced exchange coupling between the FePt grains. Since the crystallographic texture and other microstructural features are essentially the same for all of the samples, the continuity of the FePt layers is the only recognizable microstructural difference in these annealed FePt/MgO multilayers. Therefore, it is reasonable to conclude that the continuity of the FePt layers influences the magnetic properties of these annealed thin films. For the films with thinner FePt layers, the discontinuity of the magnetic layers reduces the exchange coupling between the FePt grains and thereby higher coercivity is observed. On the other hand, the low coercivity in the films with thicker FePt layers is due to the greater exchange coupling between the grains in the more-continuous magnetic layers.

CHAPTER VI

CONCLUSIONS

Highly [001] textured FePt multilayered thin films were obtained using MgO seedlayers and FePt/MgO laminations. Post-deposition annealing at 700^{o}C for 30 minutes successfully transformed the FePt layers from the disordered FCC phase to the $L1_0$-ordered phase. However, although the annealing treatment produced discontinuities in the FePt layers for a layer thickness of 2.5 nm, these FePt layers did not transform into a granular microstructure. All of the annealed films exhibit large coercivities above 6.5 kOe and high squareness ratios close to unity due to the formation of the highly anisotropic $L1_0$-ordered phase which has a strong [001] texture normal to the film plane. A reduction in coercivity as increasing FePt layer thickness is attributed to the difference in the microstructure formed after annealing. The discontinuous FePt layers are found to be responsible for the increased coercivity of the films with thinner FePt layers due to a reduction in the inter-granular exchange coupling. As the FePt layer thickness increases, annealing only coarsens the FePt layer. The FePt grains are more highly exchange coupled in the more-continuous magnetic layer with correspondingly lower coercivity. Therefore, the FePt/MgO multilayers investigated in this research are not attractive for use as recording media since the strongly exchange coupled magnetic grains cannot provide sufficient read-back SNR for high-density magnetic recording.

REFERENCES

[1] Toshiba Press, June, 2006
(http://www.toshiba.co.jp/about/press/2006_06/pr0501.htm)

[2] B. D. Cullity, Introduction to Magnetic Materials, Addison-Wesley in Metallurgy and Materials, 1972

[3] C. F. Brucker and T. W. McDaniel, Materials Development for Thermally-Assisted Magnetic Recording Media, Mat. Res. Soc. Symp. Proc., vol. 674, p. v231, 2001

[4] M. Futamoto, N. Inaba, Y. Hirayama, K. Ito and Y. Honda, Microstructure and Isomagnetics of Future Thin Film Media, J. Magn. Magn. Mater., vol. 193, p. 36, 1999

[5] M. Doerner, T. Yogi, D. Parker, S. Lambert, B. Hermsmeier, O. Allegranza and T. Nguyen, Composition Effects in High Density CoPtCr Media, IEEE Trans. Magn., vol. 29, p. 3667, 1993

[6] J. Wittig, T. Nolan, C. Ross, K. Tang, R. Sinclair and J. Bentley, Chromium Segregation in CoCrTa/Cr and CoCrPt/Cr Thin Films for Longitudinal Recording Media, IEEE Trans. Magn., vol. 34, p.1564, 1998

[7] K. Tang, M. Schabes, C. Ross, L. He, R. Ranjan, T. Yamashita and R. Sinclair, Magnetic Clusters, Intergranular Exchange Interaction and Their Micostructural Basis in Thin Films Longitudinal Media, IEEE Trans. Magn., vol. 33, p. 4074, 1997

[8] http://www.toshiba.co.jp/about/press/2004_12/pr1401.htm

[9] S. Charap, P. Lu, Y. He, Thermal Stability of Recorded Information at High Densities , IEEE Trans. Magn., vol. 33, p. 978, 1997

[10] Moser, D. Weller, Thermal Processes and Stability of Longitudinal Magnetic Recording Media, IEEE Trans. Magn., vol. 35, p. 2808, 1999

[11] M. Doerner, K. Tang, T. Arnoldussen, H. Zeng, F. Toney, D. Weller, Microstructure and Thermal Stability of Advanced Longitudinal Media, IEEE Trans. Magn., vol. 36, p. 43, 2000

[12] P. Dova, H. Laidler, and K. O'Grady, M. Toney, M. Doerner, Effects of stacking faults on magnetic viscosity in thin film magnetic recording media, J. Appl. Phys., vol. 85, p. 2775, 1999

[13] D. Weller, A. Moser, L. Folks, E. Best, W. Lee, M. Toney, M. Schwickert, J. Thiele, M. Doerner, High K_u Materials Approach to 100 Gbits/in^2, IEEE Trans. Magn., vol. 36, p. 10, 2000

[14] T. Shimatsu, H. Uwazumi, H. Muraoka and Y. Nakamura, Thermal Stability in Perpendicular Recording Media, J. Magn. Magn. Mater., vol.235, p. 273, 2001

[15] Y. Ikeda, Y. Sonobe, G. Zeltzer, B. K. Yen, K. Takano, H. Do and P. Rice, Microstructure Study of CoCrPt/Ti/NiAl Perpendicular Media, J. Magn. Magn. Mater., vol. 235, p.104, 2001

[16] B. Lu, T. Klemmer, K. Wierman, G. Ju, D. Weller, A. Roy, D. Laughlin, C. Chang and R. Ranjan, Study of Stacking Faults in Co-alloy Perpendicular Media, J. Appl. Phys., vol. 91, p. 8025, 2002

[17] R. H. Victora, Wenbin Peng, Jianhua Xue and J. H. Judy, Superlattice Magnetic Recording Media: Experiment and Simulation, J. Magn. Magn. Mater., vol.235, p. 305, 2001

[18] K. Takano, G. Zeltzer, D. Weller, and E. Fullerton, $Co_{1-x}Cr_x$/Pt Multilayers as Perpendicular Recording Media, J. Appl. Phys., vol. 87, p. 6364, 2000

[19] H. Zhou, N. Bertram, M. Doerner, M. Mirzamaani, Micromagnetic Study of Longitudinal Thin Film Media: effect of Grain Size Distribution, IEEE Trans. Magn., vol. 35, p. 2712, 1999

[20] R. E. Rottmayer, S. Batra, D. Buechel, W. A. Challener, J. Hohlfeld, Y. Kubota, L. Li, B. Lu, C. Mihalcea, K. Mountfield, K. Pelhos, C. Peng, T. Rausch, M. A. Seigler, D. Weller and X. Yang, Heat-Assisted Magnetic Recording, IEEE Trans. Magn., vol. 42, p. 2417, 2006

[21] K. Matsumoto, A. Inomata and S. Hasegawa, Thermally Assisted Magnetic Recording, FUJISTU Sci. Tech. J., vol. 42, p. 158, 2006

[22] S. Batra, J. Hannay, H. Zhou and J. Goldberg, Investigations of Perpendicular Write Head Design for 1 Tb/in^2 , IEEE Trans. Magn., vol. 40, p. 319, 2004

[23] H. Katayama, S. Sawamura, Y. Ogimoto, J. Nakajima, K. Kojima, and K. Ohta, New Magnetic Recording Method Using Laser Assisted Read/Write Technologies. Proc. of Magneto-Optical Recording Int. Symp., Monterey, J. Magn. Soc. Jpn., vol. 23 (Suppl. No. S1), p. 233, 1999

[24] H. Saga, H. Nemoto, H. Sukeda, and M. Takahashi, New Recording Method Combining Thermo-Magnetic Writing and Flux Detection, Jpn. J. Appl. Phys., vol. 38, 3B, p.1839, 1999

[25] T. Klemmer, D. Hoydick, H. Okumura, B. Zhang and W. Soffa, Magnetic Hardening and Coercivity Mechanisms in $L1_0$ Ordered FePd Ferromagnets, Scr. Metall. Mater., vol. 33, p. 1793, 1995

[26] Cebollada, D. Weller, J. Sticht, G. Harp, R. Farrow, R. Marks, R. Savoy and J. C. Scott, Enhanced Magneto-optical Kerr Effect in Spontaneously Ordered FePt Alloys: Quantitative Agreement Between Theory and Experiment, Phys. Rev. B, vol. 50, p. 3419, 1994

[27] R. Ristau, K. Barmak, L. Lewis, K. Coffey and J. K. Howard, On the Relationship of High Coercivity and $L1_0$ Ordered Phase in CoPt and FePt Thin Films, J. Appl. Phys., vol. 86, p. 4527, 1999

[28] Sun, P. C. Kuo, J. Hsu, H. L. Huang, and J. M. Sun, Epitaxial Growth Mechanism of $L1_0$ FePt Thin Films on Pt/Cr Bilayer with Amorphous Glass Substrate, J. Appl. Phys., vol. 98, p. 076109, 2005

[29] Y. Shao, M. L. Yan and D. J. Sellmyer, Effects of Rapid Thermal Annealing on Nanostructure, Texture and Magnetic Properties of Granular FePt:Ag Films for Perpendicular Recording, J. Appl. Phys., vol. 93, p. 8152, 2003

[30] Y. Hsu, Sangi Jeong, D. E. Laughlin and D. N. Lambeth, The Effects of Ag Underlayer and Pt Intermediate Layers on he Microstructure and Magnetic Properties of Epitaxial FePt Thin Film, J. Magn. Magn. Matt., vol. 260, p. 282, 2003

[31] C. P. Luo, S. H. Liou, L. Gao, Y. Liu and D. J. Sellmyer, Nanostructured FePt:B_2O_3 Thin Films with Perpendicular Magnetic Anisotropy, Appl. Phys. Lett., vol. 77, p. 2225, 2000

[32] M. L. Yan, H. Zeng, N. Powers and D. J. Sellmyer, $L1_0$ (001) Oriented FePt:B_2O_3 Composite Films for Perpendicular Recording, J. Appl. Phys., vol. 91, p. 8471, 2002

[33] R. F. C. Farrow, D. Weller, R. F. Marks,M. F. Toney, A. Cebollada and G. R. Harp, Control of the Axis of Chemical Ordering and Magnetic Anisotropy in Epitaxial FePt Films, J. Appl. Phys., vol. 79, p. 5967, 1996

[34] Z. G. Zhang, K. Kang, and T. Suzuki, FePt (001) Texture Development on an Fe–Ta–C Magnetic Soft Underlayer with SiO_2/MgO as an Intermediate Layer, Appl. Phys. Lett., vol. 83, p. 1785, 2003

[35] F. T. Yuan, S. K. Chen, W. M. Liao, C. W. Hsu, S. N. Hsiao, and W. C. Chang, J. Magn. Magn. Mater., vol. 304, p. 109, 2006

[36] L. Tang and D. Laughlin, Electron Diffraction Patterns of Fibrous and Lamellar Textured Polycrystalline Thin Films. 1. Theory, J. Appl. Cryst., vol. 29, p. 411, 1996

[37] D. B. Williams and C. B. Carter, Transmission Electron Microscopy: A Textbook for Materials Science, Springer, 1996

[38] Z. Suzuki, Z. Zhang, A. K. Singh, J. Yin, A. Pernumal, and H. Osawa, Annealing Effect on Magnetic Property and Recording Performance of [FePt/MgO]n Perpendicular Magnetic Recording Media, J. Magn. Magn. Mater., vol. 286, p. 306, 2005

[39] Tu Chen, The micromagnetic propertis of high-coercivity metallic thin films and their effects on the limit of packing density in digital recording, IEEE Trans. Magn., vol. 17, p. 1181, 1981

[40] J. G. Zhu, N. H. Bertram, Recording and transition noise simulations in thin film media, IEEE Trans. Magn., vol. 24, p. 2706, 1988

[41] J. H. Judy, Experimental studies of noise in isotropic longitudinal CoCrTa/Cr thin-film media, IEEE Trans. Magn., vol. 29, p. 209, 1993

[42] M. L. Plumer, J. van Ek and D. Weller, The Physics of Ultrahigh-Density Magnetic Recording, Springer Series in Surface Sciences, 2001